Asymptotic gravitational-wave fluxes from a spinning test body on generic orbits around a Kerr black hole

Viktor Skoupý[1,2,*] Georgios Lukes-Gerakopoulos[1] Lisa V. Drummond[3] and Scott A. Hughes[3]

[1]*Astronomical Institute of the Czech Academy of Sciences,*
Boční II 1401/1a, CZ-141 00 Prague, Czech Republic
[2]*Institute of Theoretical Physics, Faculty of Mathematics and Physics,*
Charles University, CZ-180 00 Prague, Czech Republic
[3]*Department of Physics and MIT Kavli Institute, MIT, Cambridge, Massachusetts 02139, USA*

This work provides gravitational-wave energy and angular momentum asymptotic fluxes from a spinning body moving on generic orbits in a Kerr spacetime up to the linear-in-spin approximation. To achieve this, we have developed a new frequency-domain Teukolsky equation solver that calculates asymptotic amplitudes from generic orbits of spinning bodies with their spin aligned with the total orbital angular momentum. However, the energy and angular momentum fluxes from these orbits in the linear-in-spin approximation are appropriate for adiabatic models of extreme-mass-ratio inspirals even for spins nonaligned to the orbital angular momentum. To check the newly obtained fluxes, they are compared with already known frequency-domain results for equatorial orbits and with results from a time-domain Teukolsky equation solver called TEUKODE for off-equatorial orbits. The spinning-body framework of our work is based on the Mathisson-Papapetrou-Dixon equations under the Tulczyjew-Dixon spin supplementary condition.

I. INTRODUCTION

Future space-based gravitational-wave (GW) detectors, like the Laser Interferometer Space Antenna (LISA) [1], TianQin [2], and Taiji [3], are designed to detect GWs from sources emitting in the mHz bandwidth like the extreme-mass-ratio inspirals (EMRIs). An EMRI consists of a primary supermassive black hole and a secondary compact object, like a stellar-mass black hole or a neutron star, which is orbiting in close vicinity around the primary. Due to gravitational radiation reaction, the secondary slowly inspirals into the primary, while the EMRI system is emitting GWs to infinity. Since signals from EMRIs are expected to overlap with other systems concurrently emitting GWs in the mHz bandwidth [1], matched filtering will be employed for the detection and parameter estimation of the received GW signals. This method relies on comparison of the signal with GW waveform templates and, thus, these templates must be calculated in advance and with an accuracy of the GW phases up to fractions of radians [4]. With this level of accuracy, it is anticipated that the detection of GWs from EMRIs will provide an opportunity to probe in detail the strong gravitational field near a supermassive black hole [4].

Several techniques have been employed to model an EMRI system and the GWs it emits. The backbone of these techniques is the perturbation theory [5–7] in which the secondary body is treated as a point particle moving in a background spacetime. Such an approach is justified because the mass ratio $q = \mu/M$ between the mass of the secondary μ and the mass of the primary M lies between 10^{-7} and 10^{-4}. The particle acts as a source to a gravitational perturbation to the background spacetime and conversely the perturbation exerts a force on the particle [7]. After the expansion of the perturbation in q, the first-order perturbation is the source of the first-order self-force and both first- and second-order perturbations are sources of the second-order self-force. These parts of the self-force are expected to be sufficient to reach the expected accuracy needed to model an EMRI [6].

Another technique, which is widely used in EMRI modeling, is the *two-time-scale approximation* [8,9]. This approximation relies on the separation between the orbital time scale and the inspiral time scale. In an EMRI the rate of energy loss $\dot{E}$ over the energy E is $\dot{E}/E = \mathcal{O}(q)$, which implies that the time an inspiral lasts is $\mathcal{O}(q^{-1})$. Hence, the inspiraling time is much longer than the orbital time scale $\mathcal{O}(q^0)$. Moreover, since the mass ratio q is very small, the deviation from the trajectory that the secondary body would follow without the self-force is very small as well. Hence, an EMRI can be modeled as a secondary body

*skoupy@asu.cas.cz

moving on an orbit in a given spacetime background with slowly changing orbital parameters; this type of modeling is called the *adiabatic approximation* [10–13].

For a nonspinning body inspiraling into a Kerr black hole the phases of the GW can be expanded in the mass ratio as [8]

$$\Phi_\mu(t) = \frac{1}{q}\Phi_\mu^0(qt) + \Phi_\mu^1(qt) + \mathcal{O}(q), \qquad (1)$$

where the first term on the right-hand side is called the adiabatic term and the second is called the postadiabatic term. The adiabatic term can be calculated from the averaged dissipative part of the first-order self-force, while the postadiabatic term is calculated from several other parts of the self-force, namely, from the rest of the first-order self-force, i.e., the oscillating dissipative part and the conservative part, and from the averaged dissipative part of the second-order self-force [6]. To accurately model the inspiral up to radians, the postadiabatic term cannot be neglected.

So far we have discussed the case of a nonspinning secondary body; however, to accurately calculate waveforms for an EMRI, one must also include the spin of the secondary. To understand why, it is useful to normalize the spin magnitude of the secondary $S = \mathcal{O}(\mu^2)$ as $\sigma = S/(\mu M) = \mathcal{O}(q)$ [14]. For example, if the spinning body is set to be an extremal Kerr black hole, i.e., $S = \mu^2$, then $\sigma = q$. Thus, the contribution of the spin of the secondary to an EMRI evolution is of postadiabatic order.

The adiabatic term in the nonspinning case can be found from the asymptotic GW fluxes to infinity and to the horizon of the central back hole. This stems from the flux-balance laws which have been proven for the evolution of energy, angular momentum, and the Carter constant for nonspinning particles in Ref. [15]. For spinning bodies in the linear-in-spin approximation the flux-balance laws have been proven just for the energy and angular momentum fluxes in Refs. [16,17]. In the nonlinear-in-spin case the motion of a spinning body in a Kerr background is nonintegrable [14], i.e., there are more degrees of freedom than constants of motion. The authors of Ref. [18] showed that the motion of a spinning particle in a curved spacetime can be expressed by a Hamiltonian with at least five degrees of freedom. Hence, since this Hamiltonian system is autonomous, i.e., the Hamiltonian itself is a constant of motion, four other constants of motion are needed to achieve integrability. In the Kerr case, there is the energy and angular momentum along the symmetry axis for the full equations, while in the linear-in-spin approximation Rüdiger [19,20] found two quasiconserved constants of motion [21]. These quasiconserved constants can be interpreted as a projection of the spin to the orbital angular momentum and a quantity similar to the Carter

constant [22]. If the evolution of these quantities could be calculated from asymptotic fluxes, then one could calculate the influence of the secondary spin on the asymptotic GW fluxes. This, in turn, would allow us to capture the influence of the secondary spin on the GW phase for generic inspirals.

Fully relativistic GW fluxes from orbits of nonspinning particles along with the evolution of the respective inspirals were first calculated in Ref. [23] for eccentric orbits around a Schwarzschild black hole and in Ref. [24] for circular equatorial orbits around a Kerr black hole. Fluxes from eccentric orbits in the Kerr spacetime were calculated in Refs. [25,26], while the adiabatic evolution of the inspirals was presented in Ref. [10]. Fully generic fluxes from a nonspinning body were calculated in Ref. [27] and were employed in Ref. [11] to adiabatically evolve the inspirals. The spin of the secondary was included in the fluxes in Refs. [16,28–31] from circular orbits in a black hole spacetime and in the quasicircular adiabatic evolution of the orbits in Refs. [32–35]. In Ref. [17] the first-order self-force was calculated for circular orbits in the Schwarzschild spacetime. Finally, the fluxes from spinning bodies on eccentric equatorial orbits around a Kerr black hole were calculated in Ref. [36] and the adiabatic evolution in the linear-in-spin approximation was calculated in Ref. [12].

In this work, we follow the frequency-domain method to calculate generic orbits of spinning bodies around a Kerr black hole developed in Refs. [37,38] and use it to find asymptotic GW fluxes from these orbits in the case when the spin is aligned with the orbital angular momentum. The results are valid up to linear order in the secondary spin, since the orbits are only calculated up to this order.

The rest of our paper is organized as follows. Section II introduces the motion of spinning test bodies in the Kerr spacetime and describes the calculation of the linear-in-spin part of the motion in the frequency domain. Section III presents the computation of GW fluxes from the orbits calculated in Sec. II. Section IV describes the numerical techniques we employ to calculate the aforementioned orbits and fluxes, and presents comparisons of the new results with previously known equatorial-limit results and time-domain results for generic off-equatorial orbits. Finally, Sec. V summarizes our work and provides an outlook for possible extensions.

In this work, we use geometrized units where $c = G = 1$. Spacetime indices are denoted by greek letters and go from 0 to 3, null-tetrad indices are denoted by lowercase latin letters $a, b, c, \ldots$ and go from 1 to 4, and indices of the Marck tetrad are denoted by uppercase latin letters $A, B, C, \ldots$ and go from 0 to 3. A partial derivative is denoted with a comma as $U_{\mu,\nu} = \partial_\nu U_\mu$, whereas a covariant derivative is denoted by a semicolon as $U_{\mu;\nu} = \nabla_\nu U_\mu$. The Riemann tensor is defined as $R^\mu{}_{\nu\kappa\lambda} = \Gamma^\mu{}_{\nu\lambda,\kappa} - \Gamma^\mu{}_{\nu\kappa,\lambda} + \Gamma^\mu{}_{\rho\kappa}\Gamma^\rho{}_{\nu\lambda} - \Gamma^\mu{}_{\rho\lambda}\Gamma^\rho{}_{\nu\kappa}$, and the signature of the metric is $(-,+,+,+)$. The Levi-Civita

tensor $\epsilon^{\alpha\beta\gamma\delta}$ is defined as $\epsilon^{0123} = 1/\sqrt{-g}$ for rational polynomial coordinates.[1]

II. MOTION OF A SPINNING TEST BODY

The motion of an extended test body in the general relativity framework was first addressed by Mathisson in Refs. [39,40] where he introduced the concept of a "gravitational skeleton," i.e., an expansion of an extended body using its multipoles. If we wish to describe the motion of a compact object like a black hole or a neutron star, we can restrict ourselves to the pole-dipole approximation [14], where the aforementioned expansion is truncated to the dipole term and all of the higher multipoles are ignored. In this way, the extended test body is reduced to a body with spin and the respective stress-energy tensor can be written as [41]

$$T^{\mu\nu} = \int d\tau \left(P^{(\mu}v^{\nu)} \frac{\delta^4(x^\rho - z^\rho(\tau))}{\sqrt{-g}} \right.$$
$$\left. - \nabla_\alpha \left(S^{\alpha(\mu}v^{\nu)} \frac{\delta^4(x^\rho - z^\rho(\tau))}{\sqrt{-g}} \right) \right), \qquad (2)$$

where τ is the proper time, P^μ is the four-momentum, $v^\mu = dz^\mu/d\tau$ is the four-velocity, $S^{\mu\nu}$ is the spin tensor, and g is the determinant of the metric. Note that x^μ denotes an arbitrary point of the spacetime and $z^\mu(\tau)$ denotes the position of the body parametrized by the proper time.

From the conservation law $T^{\mu\nu}{}_{;\nu} = 0$, the Mathisson-Papapetrou-Dixon (MPD) equations [40,42,43] can be derived as

$$\frac{DP^\mu}{d\tau} = -\frac{1}{2} R^\mu{}_{\nu\rho\sigma} v^\nu S^{\rho\sigma}, \qquad (3a)$$

$$\frac{DS^{\mu\nu}}{d\tau} = P^\mu v^\nu - P^\nu v^\mu, \qquad (3b)$$

where $R^\mu{}_{\nu\rho\sigma}$ is the Riemann tensor. However, this system of equations is underdetermined because one has the freedom to choose the center of mass which is tracked by the solution of these equations. To close the system, a so-called spin supplementary condition (SSC) must be specified. In this work we use the Tulczyjew-Dixon (TD) [43,44] SSC

$$S^{\mu\nu} P_\mu = 0. \qquad (4)$$

Under this SSC, the mass of the body

$$\mu = \sqrt{-P^\mu P_\mu} \qquad (5)$$

and the magnitude of its spin

$$S = \sqrt{S^{\mu\nu} S_{\mu\nu}/2} \qquad (6)$$

are conserved. The relation between the four-velocity and four-momentum reads [45]

$$v^\mu = \frac{\mathsf{m}}{\mu} \left(u^\mu + \frac{\frac{1}{2} s^{\mu\nu} R_{\nu\rho\kappa\lambda} u^\rho s^{\kappa\lambda}}{1 + \frac{1}{4} R_{\alpha\beta\gamma\delta} s^{\alpha\beta} s^{\gamma\delta}} \right), \qquad (7)$$

where

$$u^\mu = \frac{P^\mu}{\mu}, \qquad s^{\mu\nu} = \frac{S^{\mu\nu}}{\mu} \qquad (8)$$

are specific momenta and $\mathsf{m} = -p^\mu v_\mu$ is a mass definition with respect to v_μ which is not conserved under the TD SSC. Note that fixing the center of mass as a reference point for the body allows us to view it as a particle. Hence, quite often the term "spinning particle" is used instead of "spinning body."

From the spin tensor $s^{\mu\nu}$ and the specific four-momentum u^μ we can define the specific spin four-vector

$$s_\mu = -\frac{1}{2} \epsilon_{\mu\nu\rho\sigma} u^\nu s^{\rho\sigma}, \qquad (9)$$

for which the evolution equation

$$\frac{Ds^\mu}{d\tau} = -u^\mu R^*_{\alpha\beta\gamma\delta} s^\alpha v^\beta u^\gamma s^\delta \qquad (10)$$

holds [46], where the right dual of the Riemann tensor has the form

$$R^*_{\alpha\beta\gamma\delta} = \frac{1}{2} R_{\alpha\beta}{}^{\mu\nu} \epsilon_{\mu\nu\gamma\delta}. \qquad (11)$$

Note that from Eq. (9) and the properties of $\epsilon_{\mu\nu\rho\sigma}$ it is clear that $s_\mu u^\mu = 0$.

In the context of an EMRI, it is convenient to define the dimensionless spin parameter

$$\sigma = \frac{S}{\mu M}, \qquad (12)$$

since one can show that σ is of the order of the mass ratio $q = \frac{\mu}{M}$ [14]. Having established that $\sigma \lesssim q$, one sees that this parameter is very small in the context of EMRI. Since the adiabatic order is calculated from the geodesic fluxes [27], every correction to the trajectory and the fluxes of the order of q influences the first postadiabatic order and higher-order corrections are pushed to second postadiabatic order and further. By taking into account that the current consensus is that for the signals observed by LISA we need

---

[1]Note that for Boyer-Lindquist coordinates the sign is opposite since the coordinate frame in Boyer-Lindquist coordinates is right-handed, whereas the coordinate frame in rational polynomial coordinates is left-handed.

an accuracy in the waveforms up to the first postadiabatic order, it is reasonable to linearize the MPD equations in the secondary spin and discard all of the terms of the order $\mathcal{O}(\sigma^2)$ and higher. Note that in Refs. [37,38] a different dimensionless spin parameter was used, which is defined as

$$s = \frac{S}{\mu^2}. \tag{13}$$

It is related to σ by $s = \sigma/q$ and its magnitude is bounded by one.

After the linearization in σ the relation (7) reads

$$v^\mu = u^\mu + \mathcal{O}(s^2) \tag{14}$$

and the MPD equations themselves simplify to

$$\frac{\mathrm{D}u^\mu}{\mathrm{d}\tau} = -\frac{1}{2}R^\mu{}_{\nu\rho\sigma}u^\nu s^{\rho\sigma}, \tag{15a}$$

$$\frac{\mathrm{D}s^{\mu\nu}}{\mathrm{d}\tau} = 0, \tag{15b}$$

and

$$\frac{\mathrm{D}s^\mu}{\mathrm{d}\tau} = 0. \tag{16}$$

Equation (16) is the equation of parallel transport along the trajectory. After rewriting this equation using the total derivative

$$\frac{\mathrm{d}s^\mu}{\mathrm{d}\tau} + \Gamma^\mu{}_{\alpha\beta}u^\alpha s^\beta = 0, \tag{17}$$

it can be seen that to keep the equation truncated to $\mathcal{O}(\sigma)$, the Christoffel symbol $\Gamma^\mu{}_{\alpha\beta}$ and the four-momentum have to be effectively taken at the geodesic limit [37]. Thus, the parallel transport of the spin has to take place along a geodesic.

A. Spinning particles in Kerr spacetime

In this work we treat the binary system as a spinning body moving on a Kerr background spacetime, whose line element in "rational polynomial" coordinates [47] reads

$$\begin{aligned}
\mathrm{d}s^2 = &-\left(1 - \frac{2Mr}{\Sigma}\right)\mathrm{d}t^2 - \frac{4aMr(1-z^2)}{\Sigma}\mathrm{d}t\mathrm{d}\phi \\
&+ \frac{(\varpi^4 - a^2\Delta(1-z^2))(1-z^2)}{\Sigma}\mathrm{d}\phi^2 \\
&+ \frac{\Sigma}{\Delta}\mathrm{d}r^2 + \frac{\Sigma}{1-z^2}\mathrm{d}z^2, \tag{18}
\end{aligned}$$

where

$$\Sigma = r^2 + a^2z^2,$$
$$\Delta = r^2 - 2Mr + a^2,$$
$$\varpi^2 = r^2 + a^2.$$

These coordinates are derived from the Boyer-Lindquist ones with $z = \cos\theta$ and are convenient for manipulations in an algebraic software such as *Mathematica*.

The outer horizon of a Kerr black hole is located at $r_+ = M + \sqrt{M^2 - a^2}$. A Kerr spacetime is equipped with two Killing vectors, $\xi^\mu_{(t)} = \delta^\mu_t$ and $\xi_{(\phi)} = \delta^\mu_\phi$, which are related to the stationarity and axisymmetry of the spacetime, respectively. Additionally, for the Kerr spacetime, there is also a Killing-Yano tensor in the form

$$\begin{aligned}
Y_{\mu\nu}\mathrm{d}x^\mu \wedge \mathrm{d}x^\nu = &\, az\mathrm{d}r \wedge (\mathrm{d}t - a(1-z^2)\mathrm{d}\phi) \\
&+ r\mathrm{d}z \wedge (a\mathrm{d}t - \varpi^2\mathrm{d}\phi), \tag{19}
\end{aligned}$$

from which a Killing tensor can be defined as

$$K_{\mu\nu} = Y_\mu{}^\kappa Y_{\nu\kappa}. \tag{20}$$

Thanks to these symmetries, there exist two constants of motion for the spinning particle in the Kerr background,

$$E = -u_\mu\xi^\mu_{(t)} + \frac{1}{2}\xi^{(t)}_{\mu;\nu}s^{\mu\nu}, \tag{21a}$$

$$J_z = u_\mu\xi^\mu_{(\phi)} - \frac{1}{2}\xi^{(\phi)}_{\mu;\nu}s^{\mu\nu}, \tag{21b}$$

which can be interpreted as the specific total energy measured at infinity and the component of the specific total angular momentum parallel to the axis of symmetry of the Kerr black hole measured at infinity, respectively.

Apart from the aforementioned constants, there are also a couple of quasiconserved quantities [19,20],

$$C_Y = Y_{\mu\nu}u^\mu s^\nu, \tag{21c}$$

$$K_R = K_{\mu\nu}u^\mu u^\nu - 2u^\mu s^{\rho\sigma}(Y_{\mu\rho;\kappa}Y^\kappa{}_\sigma + Y_{\rho\sigma;\kappa}Y^\kappa{}_\mu), \tag{21d}$$

for which it holds that

$$\frac{\mathrm{d}K_R}{\mathrm{d}\tau} = \mathcal{O}(\sigma^2), \qquad \frac{\mathrm{d}C_Y}{\mathrm{d}\tau} = \mathcal{O}(\sigma^2). \tag{22}$$

The existence of these quasiconserved quantities causes the motion of a spinning particle in a Kerr background to be nearly integrable to linear order in σ [21]. Actually, for a Schwarzschild background ($a = 0$) it has been shown that the nonintegrability effects appear at $\mathcal{O}(\sigma^2)$ [48]. K_R is analogous to the geodesic Carter constant $K = K_{\mu\nu}u^\mu u^\nu = l_\mu l^\mu$ (see Appendix A), where $l^\mu = Y_\nu{}^\mu u^\nu$ can be interpreted

as the total specific (geodesic) orbital angular momentum. Because of this, C_Y can be interpreted as a scalar product of the spin four-vector with the total orbital angular momentum. In other words, C_Y can be seen as a projection of the spin onto the total orbital angular momentum.

The four-vector l^μ was used by Marck [49] and van de Meent [50] to find a solution to a parallel transport along a geodesic in the Kerr spacetime, i.e., a solution to Eq. (16). The resulting s^μ can be written as

$$s^\mu = M(\sigma_\perp(\cos\psi_p \tilde{e}_1^\mu + \sin\psi_p \tilde{e}_2^\mu) + \sigma_\parallel e_3^\mu), \quad (23)$$

where we introduced $\sigma_\perp$ and $\sigma_\parallel$, which are decompositions of the spin four-vector to a perpendicular component and to a parallel one, respectively, to the total orbital angular momentum, while $\tilde{e}_1^\mu$, $\tilde{e}_2^\mu$, and $e_3^\mu = l^\mu/\sqrt{K}$ are the legs of the Marck tetrad [50]. (Note that the zeroth leg of the tetrad is taken to be along the four-velocity of the orbiting body: $e_0^\mu = u^\mu$. Because $s_\mu u^\mu = 0$, this tetrad leg does not appear in s^μ.) Similarly to Refs. [37,38] we define e_3^μ with opposite sign from that in Ref. [50]. The definition of C_Y implies that $\sigma_\parallel = C_Y/\sqrt{K}$.

Equation (23) describes a vector precessing around e_3^μ with precession phase ψ_p, which fulfills the evolution equation

$$\frac{d\psi_p}{d\lambda} = \sqrt{K}\left(\frac{(r^2 + a^2)E - aL_z}{K + r^2} + a\frac{L_z - a(1 - z^2)E}{K - a^2 z^2}\right), \quad (24)$$

where λ is the Carter-Mino time, related to the proper time along the orbit by $d\lambda = d\tau/\Sigma$. An analytic solution for $\psi_p(\lambda)$ can be found in Ref. [50]. The precession introduces a new frequency Υ_s into the system. Since the perpendicular component $\sigma_\perp$ is multiplied by the sine and cosine of the precession phase, the contribution of this component in the linear order is purely oscillating. Therefore, the constants of motion and the frequencies depend only on the parallel component $\sigma_\parallel$ as well as the GW fluxes of the energy and angular momentum to linear order in spin. Because of this, we neglect the perpendicular component and focus on a trajectory of a spinning body with spin aligned to the total orbital angular momentum.

B. Linearized trajectory in frequency domain

We follow the procedure of Refs. [37,38], where the bounded orbits of a spinning particle were parametrized in Mino-Carter time as

$$u_t = -\hat{E} + u_t^S(\lambda), \quad (25a)$$

$$u_\phi = \hat{L}_z + u_\phi^S(\lambda), \quad (25b)$$

$$r = \frac{p}{1 + e\cos(\Upsilon_r\lambda + \delta\hat{\chi}_r(\lambda) + \delta\chi_r^S(\lambda))} + r^S(\lambda), \quad (25c)$$

$$z = \sin I\cos(\Upsilon_z\lambda + \delta\hat{\chi}_z(\lambda) + \delta\chi_z^S(\lambda)) + z^S(\lambda), \quad (25d)$$

with

$$\Upsilon_r = \hat{\Upsilon}_r + \Upsilon_r^S,$$

$$\Upsilon_z = \hat{\Upsilon}_z + \Upsilon_z^S,$$

where the hatted quantities denote geodesic quantities and quantities with index the S are proportional to σ.[2]

This parametrization assumes that the particle oscillates between its radial and polar turning points, but, unlike in the geodesic case (described in Appendix A), the radial turning points depend on z and the polar turning points depend on r. This dependence is encoded in the corrections r^S and z^S, respectively. Υ_r and Υ_z are the radial and polar frequency, but because of the corrections r^S and z^S the radial and polar motion also has a small contribution from a combination of all of the frequencies, $n\Upsilon_r + k\Upsilon_z + j\Upsilon_s$, where n, k, and j are integers. This parametrization assumes that a reference geodesic is given by the semilatus rectum p, eccentricity e, and inclination I (see Appendix A for their definitions), and the trajectory of a spinning particle has the same turning points after averaging.

With these frequencies in hand, the quantities in Eq. (25) parametrized with respect to λ can be expanded in the frequency domain as

$$f(\lambda) = \sum_{n,k,j} f_{nkj} e^{-in\Upsilon_r\lambda - ik\Upsilon_z\lambda - ij\Upsilon_s\lambda}. \quad (26)$$

In particular, $\delta\chi_r^S$ is summed only over positive and negative n; $\delta\chi_z^S$ is summed only over positive and negative k; and k and j cannot be simultaneously zero for r^S and n and j cannot be simultaneously zero for z^S. In our numerical calculations we truncate the n and k sums at $\pm n_{max}$ and $\pm k_{max}$. These maxima are determined empirically from the convergence of contributions to the total flux from each mode, as well as from the mode's numerical properties; more details are shown in Sec. IV. The index j is summed from -1 to 1.

After introducing the phases

$$w_r = \Upsilon_r\lambda, \quad (27a)$$

$$w_z = \Upsilon_z\lambda, \quad (27b)$$

$$w_s = \Upsilon_s\lambda, \quad (27c)$$

---

[2] Υ_s does not need to be expanded to first order in σ because it appears in terms proportional to σ.

we can write the inverse expression for Eq. (26) as

$$f_{knj} = \int \frac{\mathrm{d}w_r \mathrm{d}w_z \mathrm{d}w_s}{(2\pi)^3} f(w_r, w_z, w_s) e^{inw_r + ikw_z + ijw_s}. \quad (28)$$

Equation (15a) together with the normalization of the four-velocity $u^\mu u_\mu = -1$ are then used to find the quantities (25) in the frequency domain.

The coordinates can then be linearized with fixed phases as $r(w_r, w_z, w_s) = \hat{r}(w_r) + r^S(w_r, w_z, w_s)$, $z(w_r, w_z, w_s) = \hat{z}(w_z) + z^S(w_r, w_z, w_s)$, where the linear-in-spin parts can be expressed as [37,38]

$$r^S = \frac{ep\delta\chi_r^S \sin(w_r + \delta\hat{\chi}_r)}{(1 + e\cos(w_r + \delta\hat{\chi}_r))^2} + \mathscr{r}^S, \quad (29)$$

$$z^S = -\sin I \delta\chi_z^S \sin(w_z + \delta\hat{\chi}_z) + \mathscr{z}^S. \quad (30)$$

For the calculation of GW fluxes we also need the coordinate time and azimuthal coordinate. Both can be expressed as a secularly growing part plus a purely oscillating part, i.e.,

$$t = \Gamma\lambda + \Delta t(\Upsilon_r \lambda, \Upsilon_z \lambda, \Upsilon_s \lambda), \quad (31)$$

$$\phi = \Upsilon_\phi \lambda + \Delta\phi(\Upsilon_r \lambda, \Upsilon_z \lambda, \Upsilon_s \lambda), \quad (32)$$

where the oscillating parts Δt and $\Delta\phi$ cannot be separated, unlike in the geodesic case in Eq. (A6) where they are broken up into r and z parts [51]. These oscillating parts can be calculated from the four-velocity with respect to Carter-Mino time, $U^\mu \equiv \mathrm{d}x^\mu/\mathrm{d}\lambda = \Sigma u^\mu \equiv \Sigma \mathrm{d}x^\mu/\mathrm{d}\tau$. After integrating

$$\frac{\mathrm{d}t}{\mathrm{d}\lambda} = U^t = \sum_{n,k,j} U_{nkj}^t e^{-in\Upsilon_r \lambda - ik\Upsilon_z \lambda - ij\Upsilon_s \lambda}, \quad (33)$$

the n, k, j mode of $\Delta t(\lambda)$ in the frequency domain (26) reads

$$\Delta t_{nkj} = \frac{U_{nkj}^t}{-in\Upsilon_r - ik\Upsilon_z - ij\Upsilon_s}, \quad (34)$$

where U_{nkj}^t is the harmonic mode of the four-velocity. By linearizing the above equation in spin, we obtain

$$\Delta t_{nkj}^S = \frac{iU_{S,nkj}^t}{n\hat{\Upsilon}_r + k\hat{\Upsilon}_z + j\Upsilon_s} - \frac{i\hat{U}_{nkj}^t(n\Upsilon_r^S + k\Upsilon_z^S)}{(n\hat{\Upsilon}_r + k\hat{\Upsilon}_z)^2}. \quad (35)$$

The second term is zero for $j = \pm 1$ and Υ_s^S is not needed, since the geodesic motion is independent of Υ_s. The linear-in-spin part of the t component of the four-velocity can be expressed as

$$U_S^t = \frac{\partial V^t}{\partial r} r^S + \frac{\partial V^t}{\partial z} z^S - \frac{\partial V^t}{\partial E} u_t^S + \frac{\partial V^t}{\partial L_z} u_\phi^S, \quad (36)$$

where V^t is given in Eq. (A5a). Similarly as for $\Delta\phi^S$, we use U^ϕ to get $\Delta\phi_{nkj}$ and consequently $\Delta\phi_{nkj}^S$, in which U_S^ϕ is as in Eq. (36), but instead of V^t we use V^ϕ.

The linear-in-spin parts of Γ and ϕ are $U_{S,000}^t$ and $U_{S,000}^\phi$, respectively [38]. The coordinate-time frequencies read

$$\Omega_r = \frac{\hat{\Upsilon}_r + \Upsilon_r^S}{\hat{\Gamma} + \Gamma^S}, \quad (37a)$$

$$\Omega_z = \frac{\hat{\Upsilon}_z + \Upsilon_z^S}{\hat{\Gamma} + \Gamma^S}, \quad (37b)$$

$$\Omega_\phi = \frac{\hat{\Upsilon}_\phi + \Upsilon_\phi^S}{\hat{\Gamma} + \Gamma^S}, \quad (37c)$$

$$\Omega_s = \frac{\hat{\Upsilon}_s}{\hat{\Gamma} + \Gamma^S}. \quad (37d)$$

III. GRAVITATIONAL-WAVE FLUXES

In this work we calculate the GWs generated by a spinning particle moving on a generic orbit around a Kerr black hole using the Newman-Penrose (NP) formalism. We calculate a perturbation of the NP scalar

$$\Psi_4 = -C_{\alpha\beta\gamma\delta} n^\alpha \bar{m}^\beta n^\gamma \bar{m}^\delta, \quad (38)$$

where $C_{\alpha\beta\gamma\delta}$ is the Weyl tensor and n^μ and $\bar{m}^\mu$ are part of the Kinnersley tetrad $(\lambda_1^\mu, \lambda_2^\mu, \lambda_3^\mu, \lambda_4^\mu) = (l^\mu, n^\mu, m^\mu, \bar{m}^\mu)$ defined as

$$l^\mu = \left(\frac{r^2 + a^2}{\Delta}, 1, 0, \frac{a}{\Delta}\right), \quad (39a)$$

$$n^\mu = \frac{1}{2\Sigma}(\varpi^2, -\Delta, 0, a), \quad (39b)$$

$$m^\mu = \frac{\sqrt{1 - z^2}}{\sqrt{2}\bar{\zeta}}\left(ia, 0, -1, \frac{i}{1 - z^2}\right), \quad (39c)$$

$$\bar{m}^\mu = \frac{\sqrt{1 - z^2}}{\sqrt{2}\zeta}\left(-ia, 0, -1, -\frac{i}{1 - z^2}\right), \quad (39d)$$

with

$$\zeta = r - iaz.$$

From the NP scalar (38) we can calculate the strain at infinity using the equation

$$\Psi_4(r \to \infty) = \frac{1}{2}\frac{d^2 h}{dt^2}, \qquad (40)$$

where $h = h_+ - i h_\times$ is expressed using the two polarizations of the GW. The NP scalar Ψ_4 can be found using the Teukolsky equation [52],

$$_{-2}\mathcal{O}_{-2}\psi(t, r, \theta, \phi) = 4\pi\Sigma T, \qquad (41)$$

where $_{-2}\psi = \zeta^4\Psi_4$, $_{-2}\mathcal{O}$ is a second-order differential operator and T is the source term defined from $T^{\mu\nu}$.

We solve the Eq. (41) in frequency domain, where it can be decomposed as

$$_{-2}\psi = \sum_{l,m}^\infty \frac{1}{2\pi}\int_{-\infty}^\infty d\omega \psi_{lm\omega}(r)_{-2}S_{lm}^{a\omega}(z)e^{-i\omega t + im\phi}. \quad (42)$$

Then, Eq. (41) can be separated into two ordinary differential equations, one for the radial part $\psi_{lm\omega}(r)$ and one for the angular part $_{-2}S_{lm}^{a\omega}(z)$, which is called the spin-weighted spheroidal harmonics and is normalized as

$$\int_{-1}^1 |_{-2}S_{lm}^{a\omega}(z)|^2 dz = \frac{1}{2\pi}. \qquad (43)$$

The radial equation reads

$$\mathcal{D}_{lm\omega}\psi_{lm\omega}(r) = \mathcal{T}_{lm\omega}, \qquad (44)$$

where $\mathcal{D}_{lm\omega}$ is a second-order differential operator that depends on r, and $\mathcal{T}_{lm\omega}$ is the source term which we will describe later. Because the source term is zero around the horizon and infinity, the function $\psi_{lm\omega}(r)$ must satisfy boundary conditions at these points for the vacuum case that read [11]

$$\psi_{lm\omega}(r) \approx C_{lm\omega}^+ r^3 e^{i\omega r^*}, \qquad r \to \infty, \qquad (45a)$$

$$\psi_{lm\omega}(r) \approx C_{lm\omega}^- \Delta e^{-ik_{\mathcal{H}} r^*}, \qquad r \to r_+, \qquad (45b)$$

where $k_{\mathcal{H}} = \omega - ma/(2Mr_+)$ is the frequency at the horizon and $r^* = \int \varpi^2/\Delta \, dr$ is the tortoise coordinate. The amplitudes at infinity and at the horizon $C_{lm\omega}^\pm$ can be determined using the Green function formalism as

$$C_{lm\omega}^\pm = \frac{1}{W}\int_{r_+}^\infty \frac{R_{lm\omega}^\mp \mathcal{T}_{lm\omega}}{\Delta^2}\,dr, \qquad (46)$$

where $R_{lm\omega}^\mp(r)$ are the solutions of the homogeneous radial Teukolsky equation satisfying boundary conditions at the horizon and infinity, respectively, and $W = ((\partial_r R_{lm\omega}^+)R_{lm\omega}^- - R_{lm\omega}^+\partial_r R_{lm\omega}^-)/\Delta$ is the invariant Wronskian.

According to Ref. [32], the source term can be written as

$$\mathcal{T}_{lm\omega} = \int dt d\theta d\phi \Delta^2 \sum_{ab}\mathcal{T}_{ab}e^{i\omega t - im\phi}, \qquad (47)$$

where $ab = nn, n\bar{m}, \bar{m}\bar{m}$ and

$$\mathcal{T}_{ab} = \sum_{i=0}^{I_{ab}}\frac{\partial^i}{\partial r^i}\left(f_{ab}^{(i)}\sqrt{-g}T_{ab}\right), \qquad (48)$$

with $I_{nn} = 0$, $I_{n\bar{m}} = 1$, $I_{\bar{m}\bar{m}} = 2$. Note that the functions $f_{ab}^{(i)}$ (defined in Appendix B) are slightly different than the definition in Ref. [32]. The projection of the stress-energy tensor into the tetrad can be written as [53]

$$\sqrt{-g}T_{ab} = \int d\tau((A_{ab}^m + A_{ab}^d)\delta^4 - \partial_\rho(B_{ab}^\rho\delta^4)), \quad (49a)$$

where

$$A_{ab}^m = P_{(a}v_{b)}, \qquad (49b)$$

$$A_{ab}^d = S^{cd}v_{(b}\gamma_{a)dc} + S^c_{\ (a}\gamma_{b)dc}v^d, \qquad (49c)$$

$$B_{ab}^\rho = S^\rho_{\ (a}v_{b)}, \qquad (49d)$$

and the spin coefficients are defined as

$$\gamma_{adc} = \lambda_{a\mu;\rho}\lambda_d^\mu\lambda_c^\rho. \qquad (50)$$

After substituting Eqs. (47)–(49) into Eq. (46) and integrating over the delta functions, the amplitudes $C_{lm\omega}^\pm$ can be computed as

$$C_{lm\omega}^\pm = \int_{-\infty}^\infty \frac{d\tau}{\Sigma}e^{i\omega t(\tau) - im\phi(\tau)}I_{lm\omega}^\pm(r(\tau), z(\tau), u_a(\tau), S_{ab}(\tau)),$$
$$(51)$$

where $I_{lm\omega}^\pm$ is defined as

$$I_{lm\omega}^+ = \frac{\Sigma}{W}\sum_{ab}\sum_{i=0}^{I_{ab}}(-1)^i\left(\left((A_{ab}^m + A_{ab}^d + i(\omega B_{ab}^t - m B_{ab}^\phi))f_{ab}^{(i)} + B_{ab}^r\frac{\partial f_{ab}^{(i)}}{\partial r} + B_{ab}^z\frac{\partial f_{ab}^{(i)}}{\partial z}\right)\frac{d^i R_{lm\omega}^\mp}{dr^i} + B_{ab}^r f_{ab}^{(i)}\frac{d^{i+1}R_{lm\omega}^\mp}{dr^{i+1}}\right). \qquad (52)$$

Explicit expressions for A_{ab}^m, A_{ab}^d, and B_{ab}^μ are given in Appendix B.

Following a similar procedure as in Ref. [27], it can be proven that the amplitudes can be written as a sum over discrete frequencies,

$$C_{lm\omega}^{\pm} = \sum_{m,n,k,j} C_{lmnkj}^{\pm} \delta(\omega - \omega_{mnkj}) \quad \text{with}$$

$$\omega_{mnkj} = m\Omega_\phi + n\Omega_r + k\Omega_z + j\Omega_s. \tag{53}$$

The partial amplitudes are given by

$$C_{lmnkj}^{\pm} = \frac{1}{(2\pi)^2 \Gamma} \int_0^{2\pi} dw_r \int_0^{2\pi} dw_z \int_0^{2\pi} dw_s I_{lmnkj}^{\pm}(w_r, w_z, w_s)$$

$$\times \exp(i\omega_{mnkj}\Delta t(w_r, w_z, w_s) - im\Delta\phi(w_r, w_z, w_s) + inw_r + ikw_z + ijw_s), \tag{54}$$

where $I_{lmnkj}^{\pm}(w_r, w_z, w_s) = I_{lm\omega_{mnkj}}^{\pm}(r(w_r, w_z, w_s), z(w_r, w_z, w_s), u_a(w_r, w_z, w_s), S_{ab}(w_r, w_z, w_s))$.

The strain at infinity can be expressed from Eq. (40) as

$$h = -\frac{2}{r} \sum_{l,m,n,k,j} \frac{C_{lmnkj}^{+}}{\omega_{mnkj}^2} S_{lmnkj}(\theta) e^{-i\omega_{mnkj}u + im\phi}, \tag{55}$$

where $u = t - r^*$ is the retarded coordinate and $S_{lmnkj}(\theta) = {}_{-2}S_{lm}^{a\omega_{mnkj}}(\theta)$.

From the strain h and the stress-energy tensor of a GW, the averaged energy and angular momentum fluxes can be derived as

$$\langle \mathcal{F}^E \rangle = \sum_{l,m,n,k,j} \mathcal{F}_{lmnkj}^E, \tag{56a}$$

$$\langle \mathcal{F}^{J_z} \rangle = \sum_{l,m,n,k,j} \mathcal{F}_{lmnkj}^{J_z}, \tag{56b}$$

with

$$\mathcal{F}_{lmnkj}^E = \frac{|C_{lmnkj}^{+}|^2 + \alpha_{lmnkj}|C_{lmnkj}^{-}|^2}{4\pi\omega_{mnkj}^2}, \tag{56c}$$

$$\mathcal{F}_{lmnkj}^{J_z} = \frac{m\left(|C_{lmnkj}^{+}|^2 + \alpha_{lmnkj}|C_{lmnkj}^{-}|^2\right)}{4\pi\omega_{mnkj}^3}, \tag{56d}$$

where

$$\alpha_{lmnkj} = \frac{256(2Mr_+)^5 k_{\mathcal{H}}(k_{\mathcal{H}}^2 + 4\epsilon^2)(k_{\mathcal{H}}^2 + 16\epsilon^2)\omega_{mnkj}^3}{|\mathcal{C}_{lm\omega_{mnkj}}|^2}, \tag{57}$$

$\epsilon = \sqrt{M^2 - a^2}/(4Mr_+)$, and the Teukolsky-Starobinsky constant is

$$|\mathcal{C}_{lm\omega}|^2 = ((\lambda_{lm\omega} + 2)^2 + 4a\omega(m - a\omega))$$
$$\times (\lambda_{lm\omega}^2 + 36a\omega(m - a\omega))$$
$$- (2\lambda_{lm\omega} + 3)(48a\omega(m - 2a\omega))$$
$$+ 144\omega^2(M^2 - a^2). \tag{58}$$

Since all of the terms proportional to the perpendicular component $\sigma_\perp$ are purely oscillating with frequency Ω_s, the only contribution to the fluxes from $\sigma_\perp$ comes from the modes with $j = \pm 1$. The amplitudes $C_{lmnkj}^{\pm}$ for $j = \pm 1$ are proportional to $\sigma_\perp$ and, therefore, the fluxes for $j = \pm 1$ are quadratic in $\sigma_\perp$. We can neglect them in the linear order in σ and sum over l, m, n, and k with $j = 0$. In this work we focus on the contribution of the parallel component $\sigma_\parallel$ to the fluxes and, therefore, calculate only the $j = 0$ modes. For simplicity, in the rest of the article we omit the j index and write ω_{mnk}, $\mathcal{F}_{lmnk}$.

Note that since the trajectory is computed up to linear order in σ, the amplitudes or the fluxes are valid up to $\mathcal{O}(\sigma)$ as well.

IV. NUMERICAL IMPLEMENTATION AND RESULTS

In this section we describe the process of numerically calculating the orbit and fluxes described in the previous sections. If not stated otherwise, all calculations are done in *Mathematica*. In some parts of these calculations we use the BLACK HOLE PERTURBATION TOOLKIT (BHPT) [54].

A. Calculating the trajectory

Our approach to calculating the linear-in-spin parts of the trajectory is the same as the approach described in Refs. [37,38]. We managed to simplify the equations given in these papers, and the respective details are given in Appendix C. To calculate the geodesic motion we employ the KERRGEODESICS package of BHPT.

Using the aforementioned simplifications, we first calculate $u_{t,nk}^S$ and $u_{\phi,nk}^S$ as

$$u_{t,nk}^S = \frac{i\mathcal{R}_{t,nk}}{n\hat{\Upsilon}_r + k\hat{\Upsilon}_z}, \qquad u_{\phi,nk}^S = \frac{i\mathcal{R}_{\phi,nk}}{n\hat{\Upsilon}_r + k\hat{\Upsilon}_z} \quad (59)$$

for $n \neq 0$ or $k \neq 0$, where $\mathcal{R}_{t,nk}$ and $\mathcal{R}_{\phi,nk}$ are Fourier coefficients of the functions given in Eq. (C5). Then, the Fourier coefficients $u_{t,00}^S$, $u_{\phi,00}^S$, $\delta\chi_{r,n}^S$, $\delta\chi_{z,k}^S$, r_{nk}^S, z_{nk}^S and the frequencies' components $\hat{\Upsilon}_r^S$, and $\hat{\Upsilon}_z^S$ are calculated as the least-squares solution to the system of linear equations [37]

$$\mathbf{M} \cdot \mathbf{v} + \mathbf{c} = 0. \quad (60)$$

In the system of equations (60), the column vector $\mathbf{v}$ contains the unknown coefficients, the column vector $\mathbf{c}$ is given by the Fourier expansion components of the functions $\mathcal{J}$, $\mathcal{V}$, and $\mathcal{P}$ in Eq. (C5) that are not coefficients of the unknown quantities, and the elements of the matrix $\mathbf{M}$ are calculated from the Fourier coefficients of the functions $\mathcal{F}_{r,r}$, $\mathcal{G}_{r,r,\theta,z}$, $\mathcal{H}_{r,r,\theta,z}$, $\mathcal{I}_{1r,1\theta,2,3}$, $\mathcal{Q}_{\theta,z}$, $\mathcal{S}_{r,r,\theta,z}$, $\mathcal{T}_{r,r,\theta,z}$, $\mathcal{U}_{1r,1\theta,2,3}$, $\mathcal{K}_{r,r,\theta,z}$, $\mathcal{M}_{r,r,\theta,z}$, $\mathcal{N}_{1r,1\theta}$, which are functions of the geodesic quantities and are given in the supplemental material of Ref. [37].

In particular, the Fourier coefficients are calculated as, e.g.,

$$\mathcal{R}_{t,nk} = \sum_{a,b} \mathcal{R}_t(\hat{r}(w_r^a), \hat{z}(w_z^b)) F_n^a G_k^b, \quad (61)$$

where F_n^a and G_k^b are matrices of a discrete Fourier transform,

$$F_n^a = \exp\left(\frac{\pi i n}{N_r}(1 + 2a)\right)\frac{1}{N_r}, \quad (62a)$$

$$G_k^b = \exp\left(\frac{\pi i k}{N_z}(1 + 2b)\right)\frac{1}{N_z}, \quad (62b)$$

and N_r (N_z) is the number of points along w_r (w_z). Each function $\mathcal{R}_t$ is evaluated at equidistant points along w_r and w_z as

$$w_r^a = \frac{2\pi}{N_r}\left(\frac{1}{2} + a\right), \quad (63a)$$

$$w_z^b = \frac{2\pi}{N_z}\left(\frac{1}{2} + b\right), \quad (63b)$$

where $a = 0, 1, \ldots, N_r - 1$, $b = 0, 1, \ldots, N_z - 1$. The numbers of steps along w_r and w_z are chosen according to the orbital parameters, i.e., a higher number of steps is needed for higher eccentricity and higher inclination.

Actually, not all of the Fourier coefficients can be calculated accurately enough for highly eccentric and inclined orbits, as can be seen in Fig. 1, where the
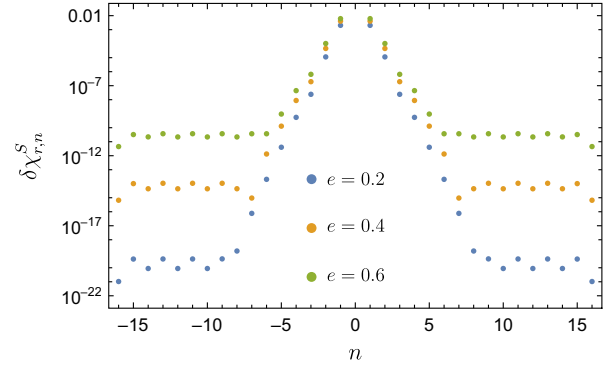

FIG. 1. Fourier coefficients $\delta\chi_{r,n}^S$ for generic orbits with $a = 0.9M$, $p = 15$, $I = 15°$, and different eccentricities. Because the Fourier series is truncated at $n_{\max} = 16$ and the coefficients are calculated approximately using least squares, the convergence stops at certain $\pm n$.

coefficients $\delta\chi_{r,n}^S$ are plotted for different eccentricities. Figure 1 shows that after a certain value of n the coefficients stop decreasing. This is caused by the truncation of the series and by the fact that the system of equations is solved approximately using least squares. Similar behavior occurs for $\delta\chi_{z,k}^S$ and other Fourier series.

B. Gravitational-wave fluxes

After calculating the orbit, the partial amplitudes $C_{lmnk}^{\pm}$ are evaluated by numerically calculating the two-dimensional integral (54). The integral in Eq. (54) is computed over one period of w_r and of w_z; hence, we employ the midpoint rule, since the convergence is exponential [55]. The number of steps for the integration is been chosen as follows. We assume that the main oscillating part of the integrand comes from the exponential term. The number of oscillations in w_r and w_z is n and k, respectively. However, because of Δt and $\Delta\phi$, the "frequency" of the oscillations can be higher at the turning points, as can be seen in Fig. 3 in Ref. [36]. In order to have enough steps in each oscillation, the number of steps in w_r is calculated from the frequency of the oscillations at the pericenter ($w_r = 0$) and apocenter ($w_r = \pi$) as

$$\max\{|16\lceil\varphi_r'(0) + n\rceil|, |16\lceil\varphi_r'(\pi) + n\rceil|, 32\}. \quad (64)$$

Similarly, the number of steps in w_z comes from the frequency at the turning point ($w_z = 0, \pi$) and the equatorial plane ($w_z = \pi/2$) as

$$\max\{|8\lceil\varphi_z'(0) + k\rceil|, |8\lceil\varphi_z'(\pi/2) + k\rceil|, 32\}, \quad (65)$$

where $\varphi_y(w_y) = \omega_{mnk}\Delta\hat{t}_y(w_y) - m\Delta\hat{\phi}_y(w_y)$, $y = r, z$. The integration over w_s is trivial for $j = 0$, since the function is independent of w_s.

The homogeneous radial Teukolsky equation solutions $R^{\pm}_{lmn\omega}$ have been calculated using the Teukolsky package of BHPT. There the radial Teukolsky equation is numerically integrated in hyperboloidal coordinates [56] and the initial conditions are calculated using the Mano-Sasaki-Takasugi method [57]. On the other hand, the spin-weighted spheroidal harmonics $_{-2}S^{a\omega}_{lm}$ are calculated using the SpinWeightedSpheroidalHarmonics package of BHPT, where Leaver's method [58] is employed.

Similarly as in Ref. [27], we use the symmetries of the motion to reduce the integral (54) to a sum of four integrals over $0 < w_r < \pi$, $0 < w_z < \pi$. Apart from the geodesic symmetries $\hat{y}(w_y) = \hat{y}(2\pi - w_y)$, $\Delta\hat{x}_y(w_y) = -\Delta\hat{x}_y(2\pi - w_y)$, and $U^y(w_y) = -U^y(2\pi - w_y)$, where $x = t, \phi$, $y = r, z$, we also use symmetries of the linear-in-spin parts, which read $f(w_r, w_z) = f(2\pi - w_r, 2\pi - w_z)$ for r^S and z^S and $f(w_r, w_z) = -f(2\pi - w_r, 2\pi - w_z)$ for U^r_S, U^z_S, Δt^S, and $\Delta\phi^S$. Thanks to the reflection symmetry around the equatorial plane, there is also a symmetry $f(w_r, w_z) = f(w_r, w_z + \pi)$ for r^S, U^r_S, Δt^S, and $\Delta\phi^S$ and $f(w_r, w_z) = -f(w_r, w_z + \pi)$ for z^S and U^z_S. Combining these symmetries, it is sufficient to evaluate the linear-in-spin parts only for $0 < w_r < \pi$, $0 < w_z < \pi$, which reduces the computational costs, since the evaluation of the Fourier series (26) is slow. After these optimizations, calculating one mode takes seconds for low eccentricities, inclinations, and mode numbers, while it takes tens of seconds for high eccentricities, inclinations, and mode numbers.

To extract the linear-in-spin part of the partial amplitudes or fluxes, i.e., their derivative with respect to σ, we use the fourth-order finite-difference formula

$$f^S = \frac{\frac{1}{12}f(-2\sigma) - \frac{2}{3}f(-\sigma) + \frac{2}{3}f(\sigma) - \frac{1}{12}f(2\sigma)}{\sigma}, \quad (66)$$

where $f = C^{\pm}_{lmnk}$, $\mathcal{F}^E$, or $\mathcal{F}^{J_z}$ and $\sigma = 0.5$ in our calculations. This is necessary for comparisons with other results, since the $\mathcal{O}(\sigma^2)$ part of the fluxes is invalid due to the trajectory being linearized in spin.

Because the Fourier series (26) of the linear-in-spin part of the trajectory is truncated at $\pm n_{\max}$ and $\pm k_{\max}$, only a finite number of n and k modes of the amplitudes $C^{\pm}_{lmnk}$ and of the fluxes can be calculated accurately. In Fig. 2 we show the dependence of the absolute value of the linear-in-spin parts of the amplitudes $|C^+_{S,lmnk}|$ on n and k for different $n_{\max}$ and $k_{\max}$. The top panel shows amplitudes for an orbit with high eccentricity ($e = 0.5$). If the Fourier series in n is truncated at lower $n_{\max}$, the amplitudes stop being accurate after a certain value of n. Similarly, for an orbit with higher inclination ($I = 60°$), as shown in the bottom panel of Fig. 2, when the series is truncated at lower $k_{\max}$ the amplitudes stop converging with k. Such issues were already reported for geodesic fluxes in Ref. [59].
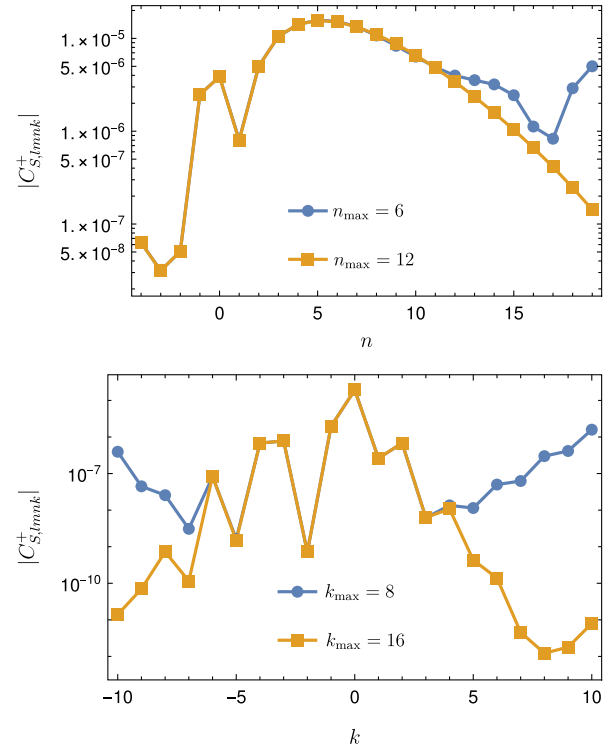

FIG. 2. Top: dependence of the linear-in-spin parts of the partial amplitudes for $k = 0$ and different $n_{\max}$ for an orbit with $a = 0.9M$, $p = 15$, $e = 0.5$, $I = 15°$. Bottom: dependence of the linear-in-spin parts of the partial amplitudes on k for $n = 0$ and different $k_{\max}$ for an orbit with $a = 0.9M$, $p = 12$, $e = 0.2$, $I = 60°$. Note that the numbers n and k refer to the modes C^+_{lmnk} and $n_{\max}$ and $k_{\max}$ refer to the trajectory.

Near the separatrix the calculations are difficult because of the divergence of some quantities, as was already shown in the equatorial case [12]. In Fig. 3 we show the dependence of $|C^+_{S,lmnk}|$ on n and k for orbits near the separatrix p_s, namely, $p - p_s = 0.19866$ for the top panel and $p - p_s = 0.22076$ for the bottom panel. We can see that Figs. 2 and 3 are qualitatively the same. This is because in both cases the dominant source of the error is the linear part of the trajectory caused by the behavior of the Fourier coefficients shown in Fig. 1. Since the coefficients $\delta\chi^S_{r,n}$, etc., are accurate only for $|n| \leq 3$ for $n_{\max} = 8$, $|n| \leq 6$ for $n_{\max} = 16$, and $|n| \leq 9$ for $n_{\mathrm{namx}} = 24$, the linear parts of the amplitudes are unreliable outside these bounds. Thus, although the linear parts of the amplitudes for $n_{\max} = 16$ and 24 seem to coincide and converge to zero, they are not trustworthy. The same arguments hold for the bottom panel of Fig. 3. For better analysis, the higher-frequency modes of the trajectory must be calculated with higher accuracy. Because this task is computationally expensive, we leave it for future work.

C. Comparison with the equatorial limit

To verify our results with the equatorial limit ($I \to 0$), we compare the frequency-domain results for several

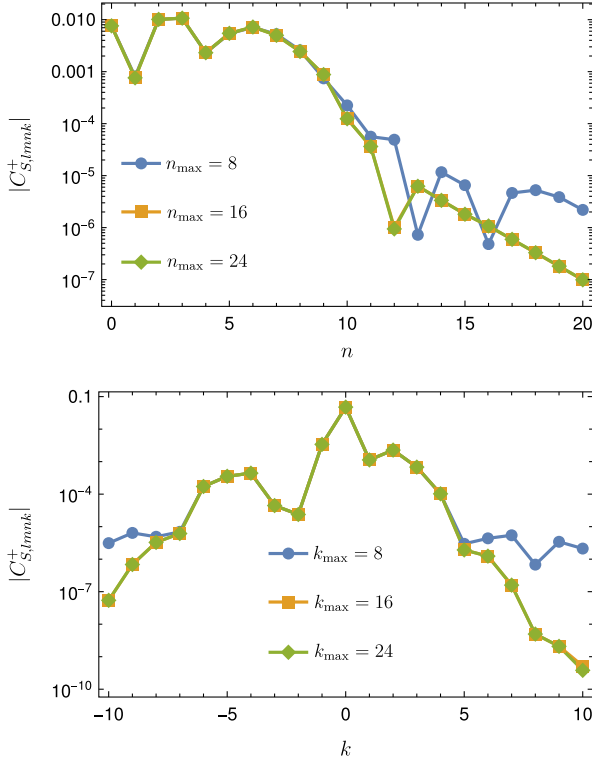FIG. 3. Dependence of the linear parts of the amplitudes on n for different n_{max} (top) and on k for different k_{max} (bottom) for orbits near the separatrix. The orbital parameters are $a = 0.9M$, $p = 3.1$, $e = 0.5$, $I = 15°$ (top) and $a = 0.9M$, $p = 4.2$, $e = 0.2$, $I = 60°$ (bottom). Note that in the top panel the $n_{max} = 16$ and $n_{max} = 24$ almost coincide; the same holds for the $k_{max} = 16$ and $k_{max} = 24$ in the bottom panel.

inclinations with a frequency-domain code for equatorial orbits [36]. First, we calculate the sum of the total energy flux over l and m for nearly spherical orbits with inclinations $I = 0.5°$, $1°$, $2°$, $4°$, $8°$. We plot the relative difference
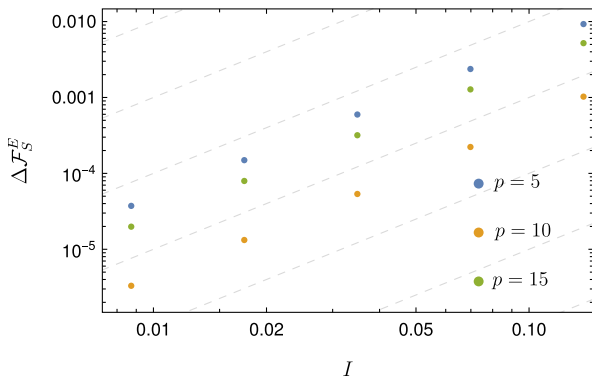

FIG. 4. Relative differences of the linear-in-spin part of the total energy flux $\mathcal{F}_S^E$ between equatorial and nearly equatorial cases of nearly spherical orbits for $a = 0.9M$ and different semilatus rectum p. The dashed gray lines indicate the $\mathcal{O}(I^2)$ behavior.
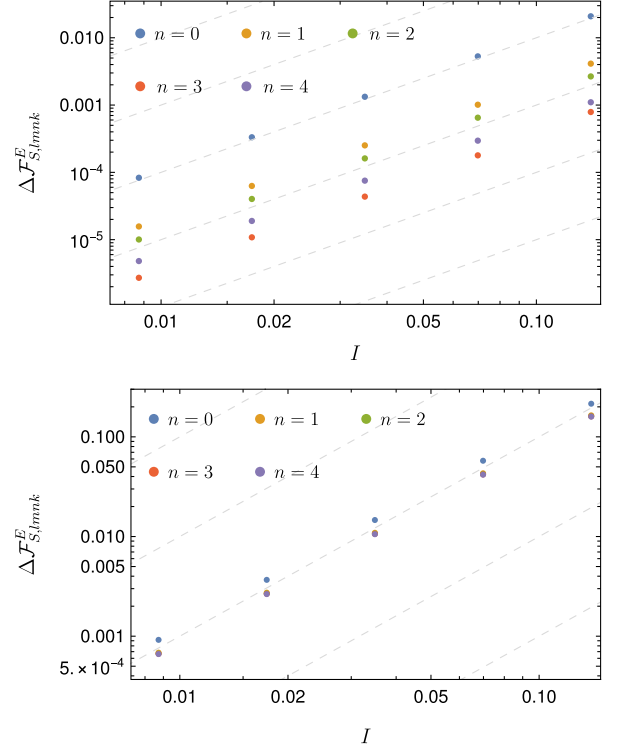

FIG. 5. Relative differences of the linear-in-spin part of the total energy flux $\mathcal{F}_{S,lmn0}^E$ between equatorial and nearly equatorial eccentric orbits with $a = 0.9M$, $p = 12$, $e = 0.3$. The top panel shows modes with $l = 2$, $m = 2$ and the bottom panel shows $l = 5$, $m = 4$. The dashed gray lines show the $\mathcal{O}(I^2)$ behavior.

$\Delta\mathcal{F}_S^E = |1 - \mathcal{F}_S^E/\mathcal{F}_{S,I=0}^E|$ against I on a logarithmic scale on both axes in Fig. 4. This way, we verify that the linear-in-spin part $\mathcal{F}_S^E$ asymptotically approaches the equatorial limit as $I \to 0$ with an $\mathcal{O}(I^2)$ difference convergence.

A similar procedure is used for the eccentric orbits. We compute the l, m, n with $k = 0$ modes of the energy flux $\mathcal{F}_{S,lmnk}^E$ for different inclinations I and plot the relative differences $\Delta\mathcal{F}_{S,lmnk}^E = |1 - \mathcal{F}_{S,lmnk}^E/\mathcal{F}_{S,lmnk,I=0}^E|$ in Fig. 5. We again see that for all of the modes the relative difference in fluxes $\mathcal{F}_{S,lmnk}^E$ follows an $\mathcal{O}(I^2)$ convergence as $I \to 0$. This behavior agrees with the behavior of a Post-Newtonian expansion of nearly equatorial geodesic fluxes in Refs. [15,60], because the parameters y and Y in these references are $\mathcal{O}(I^2)$.

D. Comparison of frequency- and time-domain results

To further verify the frequency-domain calculation of the fluxes $\mathcal{F}^E$ and $\mathcal{F}^{J_z}$, we compare them with fluxes calculated using the time-domain Teukolsky equation solver TEUKODE [61]. This code solves the $(2 + 1)$-dimensional Teukolsky equation with a spinning-particle source term in hyperboloidal horizon-penetrating coordinates. The fluxes of energy and angular momentum are extracted at the future null infinity. The numerical scheme consists of a method of
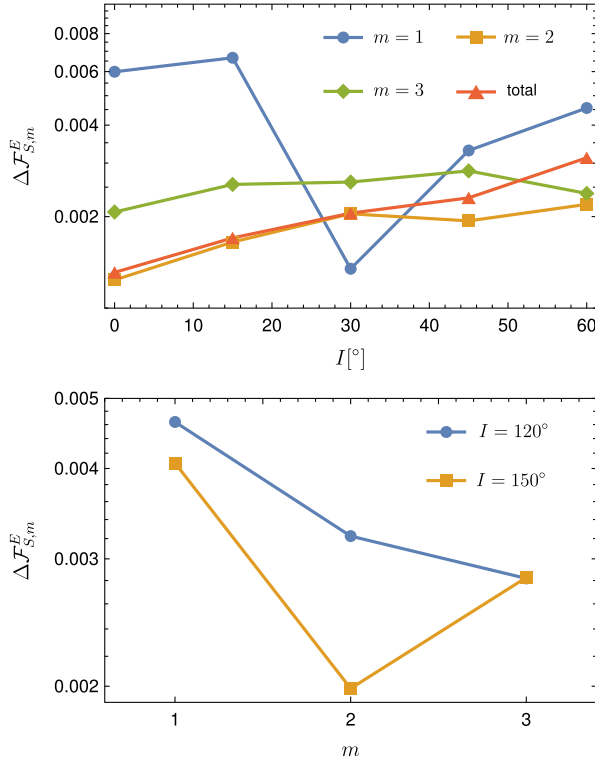
FIG. 6. Relative differences of the linear-in-spin part of the fluxes $\mathcal{F}_{S,m}^E$ between time-domain and frequency-domain calculations for different inclinations and m for nearly spherical orbits with $a = 0.9M$ and $p = 10$. The top panel shows prograde orbits and the bottom panel shows retrograde orbits.

lines with sixth-order finite-difference formulas in space and a fourth-order Runge-Kutta scheme in time.

First, we compare the computation of energy fluxes to infinity from nearly spherical orbits, i.e., orbits with $e = 0$. For details about the time-domain calculation of the trajectory and the fluxes, see Appendix D. Since the time-domain outputs m modes of the flux, we sum the frequency-domain flux over l and k (for spherical orbits, only the $n = 0$ modes are nonzero). In Fig. 6 we show the relative difference between the time-domain- and frequency-domain-computed linear-in-spin part of the energy flux $\Delta\mathcal{F}_{S,m}^E = |1 - \mathcal{F}_{S,m}^{E,\text{fd}} / \mathcal{F}_{S,m}^{E,\text{td}}|$ for several inclinations I and azimuthal numbers m. The top panel shows the dependence of the relative difference on I for prograde orbits and the lower panel shows the dependence on m for retrograde orbits. We can see that the error is at most 6×10^{-3} which is around the reported accuracy of TEUKODE in our previous paper [36]. The error of the frequency domain comes from the truncation of the Fourier expansion to $n_{\max}$ and $k_{\max}$ and from the summation of the fluxes over l and k. On top of that, one has to take into account that based on the order of the method and the length of the step we estimate that the relative error of linearization of both the time-domain and frequency-domain flux using the fourth-order finite-difference formula should be around

TABLE I. Relative differences $\Delta\mathcal{F}_{S,m}^E$ of the linear-in-spin part of the energy flux $\mathcal{F}_{S,m}^E$ between frequency-domain and time-domain computations for given orbital parameters and azimuthal number m. All orbits have $a = 0.9M$.

p	e	$I/°$	m	$\mathcal{F}_{S,m}^E$	$\Delta\mathcal{F}_{S,m}^E$
10	0.1	15	2	-2.8259×10^{-6}	1×10^{-3}
12	0.2	30	1	-1.1954×10^{-7}	2×10^{-5}
12	0.2	30	2	-1.0488×10^{-6}	1×10^{-3}
12	0.2	30	3	-1.4210×10^{-7}	3×10^{-3}
12	0.2	60	2	-8.0550×10^{-7}	5×10^{-4}
15	0.5	15	2	-4.2936×10^{-7}	2×10^{-3}

10^{-5}. This estimation holds not only for the nearly spherical orbits, but for the generic orbits as well.

Next we move to generic orbits. We sum the energy flux over l, n, and k for given m and orbital parameters, in order to calculate the relative difference between the linear part of frequency-domain fluxes and time-domain fluxes $\Delta\mathcal{F}_{S,m}^E$. The results are presented in Table I. In this case, the relative difference is at most 3×10^{-3}.

Appendix E shows plots of linear-in-spin calculations of the amplitudes and of the fluxes and some reference data tables.

V. SUMMARY

In this work we provided asymptotic GW fluxes from off-equatorial orbits of spinning bodies in the Kerr space-time. In our framework the spin of the small body is parallel to the orbital angular momentum and the calculations are valid up to linear order in the spin.

We employed the frequency-domain calculation of the orbits of spinning particles which was introduced in Refs. [37,38]. In this setup, the linear-in-spin part of the trajectory is solved in the frequency domain using MPD equations under the TD SSC. We extended this setup to calculate the corrections to the coordinate time Δt^S and the azimuthal coordinate $\Delta\phi^S$.

We calculated GW fluxes from the aforementioned orbits using the Teukolsky equation. To do that, we constructed the source of the Teukolsky equation for off-equatorial orbits of spinning particles for spin parallel to the orbital angular momentum. Then, by using this source, we developed a new frequency-domain inhomogeneous Teukolsky equation solver in *Mathematica*, which delivers the GW amplitudes $C_{lmnk}^\pm$ at infinity and at the horizon. Having these amplitudes allowed us to calculate the total energy and angular momentum fluxes, whose validity is up to linear order in the spin. Since at the linear order in spin the fluxes are independent of the precessing perpendicular component of the spin, our approach to compute the fluxes is sufficient for any linear-in-spin configuration.

We numerically linearized the fluxes and compared the results for nearly equatorial orbits with previously known

frequency-domain results [36] for equatorial orbits to verify their validity in the equatorial limit. We found that the difference of the off-equatorial and equatorial flux behaves as $\mathcal{O}(I^2)$. Furthermore, we compared the off-equatorial results with time-domain results obtained using the time-domain Teukolsky equation solver TEUKODE. For different orbital parameters and azimuthal numbers m the relative difference is around 10^{-3}, which is the current accuracy of computations produced by TEUKODE.

This work is part of an ongoing effort to find the postadiabatic terms [11,12,17,62–64] needed to model EMRI waveforms accurately enough for future space-based GW observatories like LISA. Our work can be extended to model adiabatic inspirals of a spinning body on generic orbits in a Kerr background as we have done for the equatorial-plane case in Ref. [12]; however, to achieve this the flux of the Carter-like constants K_R and the parallel component of the spin C_Y must be derived first. In the near future, we plan to publish the new frequency-domain Teukolsky equation solver *Mathematica* code in the BLACK HOLE PERTURBATION TOOLKIT repository.

APPENDIX A: GEODESIC MOTION IN KERR SPACETIME

In this appendix we briefly discuss aspects of geodesic motion in the Kerr spacetime.

The specific energy

$$E = -u_t \tag{A1}$$

and the specific angular momentum along the symmetry axis

$$L_z = u_\phi \tag{A2}$$

are conserved thanks to two respective Killing vectors. In Ref. [22] Carter found a third constant,

$$K = K_{\mu\nu} u^\mu u^\nu, \tag{A3}$$

and formulated the equations of motion as

$$\frac{dt}{d\lambda} = V_t(r, z, E, L_z), \tag{A4a}$$

$$\frac{dr}{d\lambda} = \pm\sqrt{R(r, E, L_z, K)}, \tag{A4b}$$

$$\frac{dz}{d\lambda} = \pm\sqrt{Z(z, E, L_z, K)}, \tag{A4c}$$

$$\frac{d\phi}{d\lambda} = V_\phi(r, z, E, L_z), \tag{A4d}$$

where

$$V^t = \frac{r^2 + a^2}{\Delta}((r^2 + a^2)E - aL_z) - a^2 E(1 - z^2) + aL_z, \tag{A5a}$$

$$R = ((r^2 + a^2)E - aL_z)^2 - \Delta(K + r^2), \tag{A5b}$$

$$Z = -((1 - z^2)aE - L_z)^2 + (1 - z^2)(K - a^2 z^2), \tag{A5c}$$

$$V^\phi = \frac{a}{\Delta}((r^2 + a^2)E - aL_z) + \frac{L_z}{1 - z^2} - aE. \tag{A5d}$$

These equations are parametrized with Carter-Mino time $d\tau/d\lambda = \Sigma$. The motion in r oscillates between its radial turning points r_1 and r_2 with frequency Υ_r and, similarly, the z motion oscillates between its polar turning points $\pm z_1$ with frequency Υ_z. Moreover, the evolution of t and ϕ can be written as

$$t(\lambda) = \Gamma\lambda + \Delta t_r(\lambda) + \Delta t_z(\lambda), \tag{A6a}$$

$$\phi(\lambda) = \Upsilon_\phi \lambda + \Delta\phi_r(\lambda) + \Delta\phi_z(\lambda), \tag{A6b}$$

where Γ and Υ_ϕ are average rates of change of t and ϕ, while Δt_r with $\Delta\phi_r$ are periodic functions with frequency Υ_r, and Δt_z with $\Delta\phi_z$ are periodic functions with frequency Υ_z.

It is convenient to define frequencies with respect to coordinate (Killing) time as

$$\Omega_r = \frac{\Upsilon_r}{\Gamma}, \tag{A7a}$$

$$\Omega_z = \frac{\Upsilon_z}{\Gamma}, \tag{A7b}$$

$$\Omega_\phi = \frac{\Upsilon_\phi}{\Gamma}, \tag{A7c}$$

but the system is not periodic in coordinate time and these frequencies should be understood as average frequencies.

The motion is often parametrized by its orbital parameters—the semilatus rectum p, eccentricity e, and inclination angle I—which are defined from the turning points as

$$r_1 = \frac{Mp}{1-e}, \qquad r_2 = \frac{Mp}{1+e}, \qquad z_1 = \sin I, \qquad \text{(A8)}$$

where $0 < I < \pi/2$ for prograde orbits and $\pi/2 < I < \pi$ for retrograde orbits. Analytic expressions for the constants of motion in terms of the orbital parameters can be found in Ref. [27]. Fujita and Hikida gave analytical expressions for the frequencies and coordinates in Ref. [51].

APPENDIX B: SOURCE TERM

In this appendix we present explicit expressions for the functions appearing in the source term for the calculation of the partial amplitudes in Eq. (52).

Whereas A_{ab}^{m} is entirely given by Eq. (49b) with $P_a = \mu u_a$ and $v_a = u_a$ in the linear order, the terms in A_{ab}^{d} can be expressed with NP spin coefficients as

$$S^{cd}\gamma_{ndc} = S_{ln}(\gamma + \bar{\gamma}) + S_{n\bar{m}}(-\bar{\pi} + \bar{\alpha} + \beta) + S_{nm}(-\pi + \alpha + \bar{\beta}) + S_{m\bar{m}}(-\mu + \bar{\mu}), \tag{B1a}$$

$$S^{cd}\gamma_{\bar{m}dc} = S_{ln}(\pi + \bar{\tau}) + S_{n\bar{m}}\bar{\rho} + S_{nm}(\alpha + \bar{\beta}) + S_{l\bar{m}}(-\bar{\gamma} + \gamma) + S_{m\bar{m}}(-\alpha + \bar{\beta}), \tag{B1b}$$

$$S^c{}_n\gamma_{ndc}u^d = S_{ln}(\gamma + \bar{\gamma})u_n + S_{n\bar{m}}((\bar{\alpha} + \beta)u_n - \mu u_m) + S_{nm}((\alpha + \bar{\beta})u_n + \bar{\mu}u_{\bar{m}}), \tag{B1c}$$

$$S^c{}_{\bar{m}}\gamma_{\bar{m}dc}u^d = S_{n\bar{m}}(-\pi u_l) + S_{l\bar{m}}(\bar{\tau}u_n - (\bar{\gamma} - \gamma)u_{\bar{m}}) - S_{m\bar{m}}(-(-\alpha + \bar{\beta})u_{\bar{m}}), \tag{B1d}$$

$$S^c{}_{(n}\gamma_{\bar{m})dc}u^d = (S_{ln}(\bar{\tau}u_n - (\bar{\gamma} - \gamma)u_{\bar{m}}) + S_{n\bar{m}}(\bar{\rho}u_n - \mu u_l - (\bar{\alpha} - \beta + \bar{\pi})u_{\bar{m}} - \pi u_m)S_{nm}(-(-\alpha + \bar{\beta})u_{\bar{m}})$$
$$+ S_{l\bar{m}}(\gamma + \bar{\gamma})u_n - S_{m\bar{m}}((\alpha + \bar{\beta})u_n - \bar{\mu}u_{\bar{m}}))/2. \tag{B1e}$$

The tetrad components of the spin tensor for $\sigma_\perp = 0$ can be expressed as

$$S_{ln} = -\sigma_\parallel \frac{r(\hat{K} - a^2 z^2)}{\sqrt{\hat{K}}\Sigma}, \qquad S_{nm} = \sigma_\parallel \frac{\zeta}{\sqrt{\hat{K}}} u_m u_n, \tag{B2a}$$

$$S_{l\bar{m}} = -\sigma_\parallel \frac{\zeta}{\sqrt{\hat{K}}} u_l u_{\bar{m}}, \qquad S_{m\bar{m}} = \sigma_\parallel \frac{iaz(\hat{K} + r^2)}{\sqrt{\hat{K}}\Sigma}, \tag{B2b}$$

while the terms from the partial derivative for the dipole term have the form

$$i(\omega S^t{}_n - m S^\phi{}_n) = \frac{a\omega(1 - z^2) - m}{\sqrt{2(1 - z^2)}\Sigma}(\zeta S_{n\bar{m}} - \bar{\zeta} S_{nm})$$
$$- \frac{iK}{2\Sigma} S_{ln}, \tag{B3a}$$

$$i(\omega S^t{}_{\bar{m}} - m S^\phi{}_{\bar{m}}) = -iK\left(\frac{S_{n\bar{m}}}{\Delta} + \frac{S_{l\bar{m}}}{2\Sigma}\right)$$
$$+ \frac{a\omega(1 - z^2) - m}{\sqrt{2(1 - z^2)}\zeta} S_{m\bar{m}}, \tag{B3b}$$

$$S^r{}_n = \frac{\Delta}{2\Sigma} S_{ln}, \tag{B3c}$$

$$S^r{}_{\bar{m}} = -S_{n\bar{m}} + \frac{\Delta}{2\Sigma} S_{l\bar{m}}, \tag{B3d}$$

$$S^z{}_n = \frac{\sqrt{1 - z^2}(S_{n\bar{m}}\zeta + S_{nm}\bar{\zeta})}{\sqrt{2}\Sigma}, \tag{B3e}$$

$$S^z{}_{\bar{m}} = -\frac{\sqrt{1 - z^2} S_{m\bar{m}}}{\sqrt{2}\zeta}, \tag{B3f}$$

where $K = (r^2 + a^2)\omega - am$. The functions $f_{ab}^{(i)}$ are given by

$$f_{nn}^{(0)} = -\frac{2\zeta^2}{\Delta^2}(\mathcal{L}_1^\dagger \mathcal{L}_2^\dagger - 2ia\zeta^{-1}\sqrt{1 - z^2}\mathcal{L}_2^\dagger)S, \tag{B4a}$$

$$f_{n\bar{m}}^{(0)} = \frac{2\sqrt{2}\zeta^2}{\bar{\zeta}\Delta}\left(\left(\frac{iK}{\Delta} + \zeta^{-1} + \bar{\zeta}^{-1}\right)\mathcal{L}_2^\dagger\right.$$
$$\left. - a\sqrt{1 - z^2}\frac{K}{\Delta}(\bar{\zeta}^{-1} - \zeta^{-1})\right)S, \tag{B4b}$$

$$f_{n\bar{m}}^{(1)} = \frac{2\sqrt{2}\zeta^2}{\bar{\zeta}\Delta}\left(\mathcal{L}_2^\dagger + ia\sqrt{1 - z^2}(\bar{\zeta}^{-1} - \zeta^{-1})\right)S, \tag{B4c}$$

$$f_{\bar{m}\bar{m}}^{(0)} = \frac{\zeta^2}{\bar{\zeta}^2}\left(i\partial_r\left(\frac{K}{\Delta}\right) - 2i\zeta^{-1}\frac{K}{\Delta} + \left(\frac{K}{\Delta}\right)^2\right)S, \tag{B4d}$$

$$f_{\bar{m}\bar{m}}^{(1)} = -\frac{2\zeta^2}{\bar{\zeta}^2}\left(\zeta^{-1} + i\frac{K}{\Delta}\right)S, \tag{B4e}$$

$$f_{\tilde{m}\tilde{m}}^{(2)} = -\frac{\zeta^2}{\bar{\zeta}^2}S, \tag{B4f}$$

where

$$\mathcal{L}_n^\dagger = -\sqrt{1-z^2}\left(\partial_z - \frac{m-nz}{1-z^2} + a\omega\right). \tag{B5}$$

APPENDIX C: TRAJECTORY

In this appendix we present some formulas we derived to calculate the linear-in-spin contribution to the trajectory.

$$R_{1012} = \frac{3\sqrt{(\hat{K}+r^2)(\hat{K}-a^2z^2)}\left(\left(a^2z^2(\hat{K}+r^2) - r^2(\hat{K}-a^2z^2)\right)I_1 + arz(2\hat{K}+r^2-a^2z^2)I_2\right)}{\hat{K}\Sigma^2}, \tag{C2a}$$

$$R_{3012} = \frac{6arz(\hat{K}+r^2)(\hat{K}-a^2z^2)I_1}{\hat{K}\Sigma^2} + \left(1 + 3\frac{-a^2z^2(\hat{K}+r^2)^2 + r^2(\hat{K}-a^2z^2)^2}{\hat{K}\Sigma^2}\right)I_2, \tag{C2b}$$

$$R_{2013} = -I_2, \tag{C2c}$$

$$R_{1023} = -R_{3012} + R_{2013}, \tag{C2d}$$

$$R_{3023} = R_{1012}, \tag{C2e}$$

and $R_{2012} = R_{1013} = R_{3013} = R_{2023} = 0$, where

$$I_1 = \frac{Mr(r^2 - 3a^2z^2)}{\Sigma^3}, \tag{C3}$$

$$I_2 = \frac{Maz(3r^2 - a^2z^2)}{\Sigma^3}. \tag{C4}$$

The functions $\mathcal{R}_{t,\phi}$, $\mathcal{J}$, $\mathcal{V}$, and $\mathcal{P}$ from Eqs. (3.24), (4.62), and (4.63) in Ref. [38] can be simplified to

$$\mathcal{R}_t = \Sigma f_t^{\text{MPD}}, \tag{C5a}$$

$$\mathcal{R}_\phi = \Sigma f_\phi^{\text{MPD}}, \tag{C5b}$$

$$\mathcal{J} = -\Sigma^2 f_{\text{MPD}}^r + \mathcal{I}_2\delta u_t^S + \mathcal{I}_3\delta u_\phi^S, \tag{C5c}$$

$$\mathcal{V} = -\Sigma^2 f_{\text{MPD}}^\theta + \mathcal{U}_2\delta u_t^S + \mathcal{U}_3\delta u_\phi^S, \tag{C5d}$$

$$\mathcal{P} = \mathcal{N}_2\delta u_t^S + \mathcal{N}_3\delta u_\phi^S, \tag{C5e}$$

where $\mathcal{I}_{2,3}$, $\mathcal{U}_{2,3}$, and $\mathcal{N}_{2,3}$ can be found in the supplemental material of Ref. [37]. These simplifications make the calculation of the trajectory significantly faster.

We use the tetrad from Eqs. (47)–(51) in Ref. [50] where $\tilde{e}_2^\mu$ and e_3^μ have opposite sign to align e_3^μ with the total angular momentum and to have a right-handed system. Then, the right-hand side of the MPD equations can be written as

$$f_{\text{MPD}}^\mu = -\frac{1}{2}e_A^\mu\eta^{AB}R_{B0CD}S^{CD}, \tag{C1}$$

where R_{B0CD} are components of the Riemann tensor in the Marck tetrad. Because of the way this tetrad is constructed [21] and the fact that the Riemann tensor has a simple form in the Kinnersley tetrad, the components can be simplified to

APPENDIX D: TRAJECTORIES AND FLUXES IN THE TIME DOMAIN

In this appendix we describe our procedure to calculate trajectories and GW fluxes in the time domain in order to compare them with the frequency-domain results.
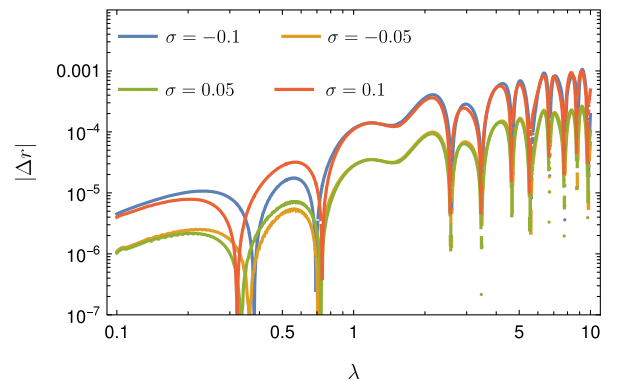
FIG. 7. Difference between the time domain calculation of r with the full MPD equations and linearized in spin frequency domain calculation of r for $a = 0.9M$, $p = 12.0$, $e = 0.2$, $I = 60°$ and different spins. The difference behaves as $\mathcal{O}(\sigma^2)$ and grows linearly in λ on average, because of the $\mathcal{O}(\sigma^2)$ difference in the frequencies.

First, we calculate the orbits using the full (nonlinearized in spin) MPD equations (3) in the time domain. The initial conditions are chosen such that the orbits are at most $\mathcal{O}(\sigma^2)$ from orbits with given orbital parameters in the frequency domain. As initial conditions we choose E, J_z, r, θ, u^r, s^r, and s^θ according to the values computed in the frequency domain. Then, we find the other initial conditions from Eqs. (4)–(6), and (21). For the evolution we use an implicit Gauss-Runge-Kutta integrator, which is described in Ref. [65]. In Fig. 7 we plot for several spins the difference

$$\Delta r = r_{\mathrm{td}}(\lambda) - \hat{r}(\Upsilon_r, \lambda) - r^S(\Upsilon_r, \lambda, \Upsilon_z, \lambda),$$

where $r_{\mathrm{td}}(\lambda)$ is the evolution computed in the time domain. It can be seen that the difference for $\sigma = \pm 0.1$ is 4 times larger than the difference for $\sigma = \pm 0.05$, and thus it is indeed $\mathcal{O}(\sigma^2)$.

This trajectory is then used as an input to TEUKODE which numerically solves the Teukolsky equation. The output is the energy flux at infinity which must be averaged to compare it with the frequency-domain result. For nearly spherical orbits it is straightforward since at linear order in spin the flux has period $2\pi/\Omega_z$. Thus, we can average the flux over several periods which have been calculated using the frequency-domain approach.

For generic orbits the averaging procedure is more challenging, since the flux is not strictly periodic and it contains contributions from all of the combinations of the frequencies Ω_r and Ω_z. This issue is resolved by consecutive moving averages with different periods. The main contribution to the oscillations of the flux comes from the radial motion between the pericenter and apocenter. Thus, we first compute the moving average of the time series with period $2\pi/\Omega_r$ to smooth out the data. Then, we perform several other moving averages with periods $2\pi/\Omega_z$ and combinations $2\pi/(n\Omega_r + k\Omega_z)$. After several such averages, the time series is too short for another moving average, so we average all of the remaining data points. This procedure appears to be reliable, since the results match the frequency-domain calculations.

APPENDIX E: PLOTS AND DATA TABLES

In this appendix we show several plots of our frequency-domain results and list the values for reference.

In Fig. 8 we plot the linear-in-spin part of the total energy flux from a nearly spherical orbit for different l, m, and k. From these plots we can see that the linear-in-spin part of the flux has a global maximum at $k = l - m$ and a local maximum around $k = -l - m$. This behavior is similar to the behavior of geodesic flux that was reported in Ref. [59].

In Fig. 9 we plot the m, n, and k modes of the linearized-in-spin flux summed over l for a generic orbit. Because of the computational costs, we calculate only some of the l, m, n, k modes. We can see that the maximal mode is at $n = 1$ and $k = 2 - m$.
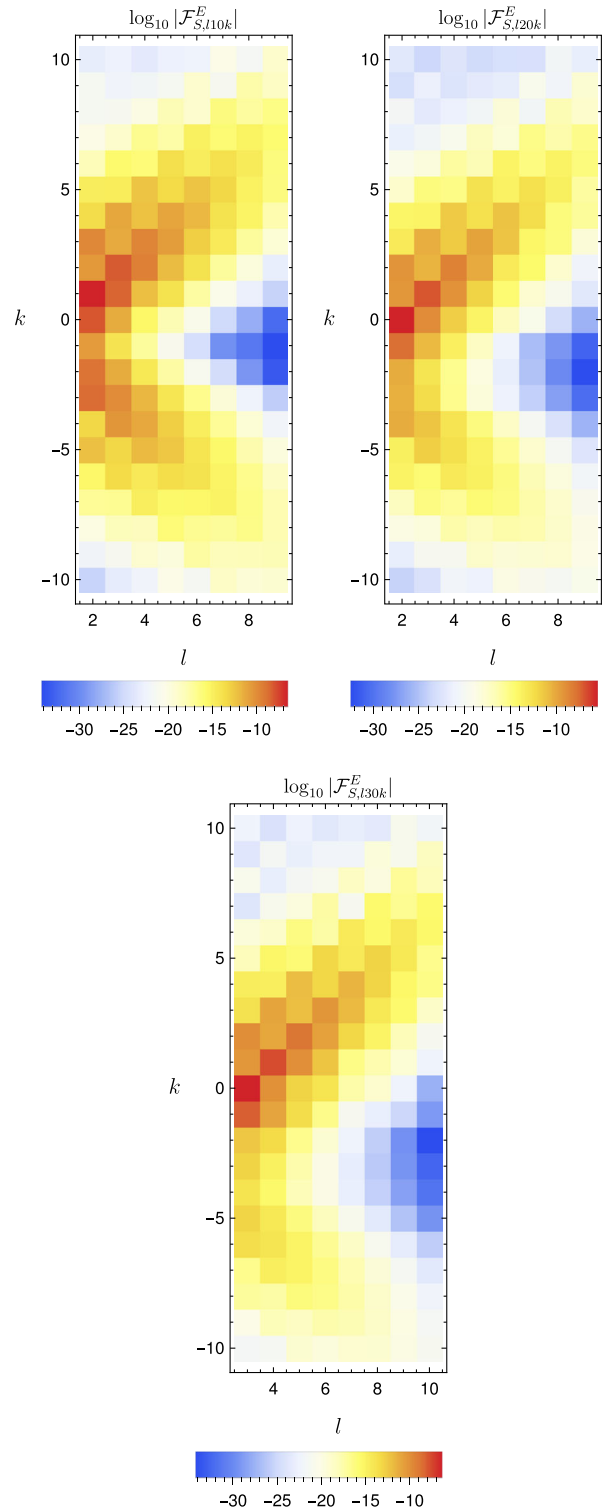

FIG. 8. Linear-in-spin parts of the energy fluxes from nearly spherical orbits with $a = 0.9M$, $p = 10.0$, $I = 30°$ for different l, k modes and $m = 1, 2, 3$.

For reference, we list the m modes of the linear-in-spin part of the energy flux for spherical orbits in Table II and some of the l, m, n, k modes from generic orbits in Table III.
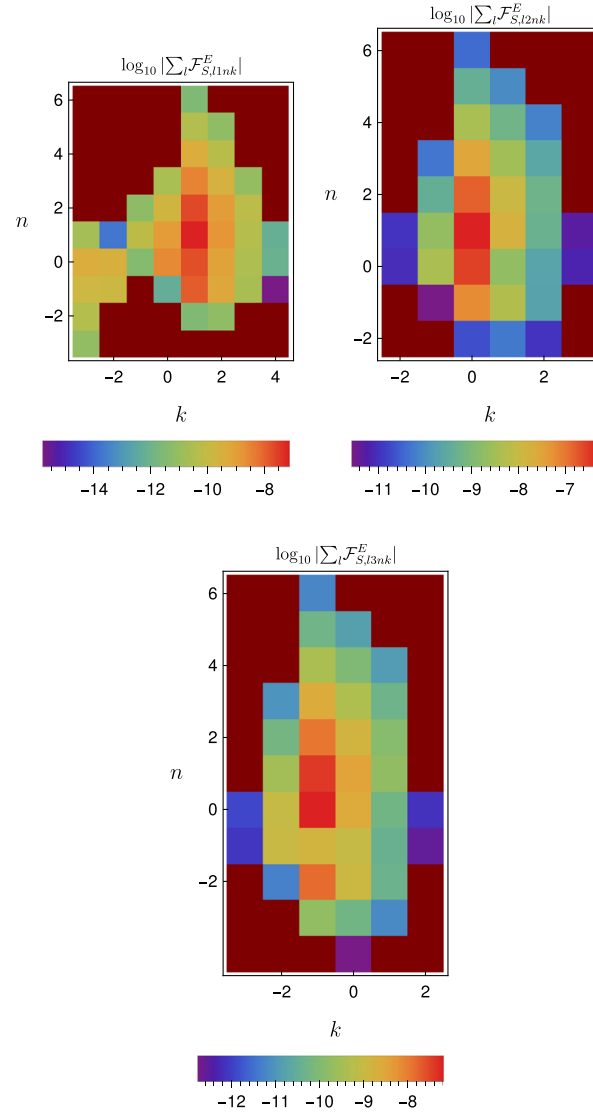
FIG. 9. Linear-in-spin parts of the energy fluxes from generic orbits $\log_{10}|\sum_l \mathcal{F}^E_{S,lmnk}|$ with $a = 0.9M$, $p = 12.0$, $e = 0.2$, $I = 30°$ for different n, k modes summed over l for $m = 1$ (top left), $m = 2$ (top right), and $m = 3$ (bottom).

TABLE II. Linear-in-spin parts of the total energy fluxes and the angular momentum fluxes from nearly spherical orbits for given inclination I and azimuthal number m. The fluxes are summed over l and k.

$I[°]$	m	$\mathcal{F}^E_{S,m}$	$\mathcal{F}^{J_z}_{S,m}$
30	1	-2.642×10^{-7}	-2.446×10^{-6}
30	2	-2.702×10^{-6}	-6.431×10^{-5}
30	3	-3.921×10^{-7}	-1.016×10^{-5}
60	1	-1.533×10^{-6}	-1.891×10^{-5}
60	2	-2.177×10^{-6}	-5.110×10^{-5}
60	3	-2.223×10^{-7}	-5.463×10^{-6}
120	1	-4.175×10^{-6}	3.021×10^{-5}
120	2	-1.796×10^{-6}	3.597×10^{-5}
120	3	-1.730×10^{-7}	4.020×10^{-6}
150	1	-2.859×10^{-6}	3.280×10^{-5}
150	2	-6.930×10^{-6}	1.658×10^{-5}
150	3	-1.069×10^{-6}	2.723×10^{-5}

TABLE III.   Real and imaginary parts of the linear-in-spin parts of amplitudes computed at infinity and at the horizon for given l, m, n, and k of a generic orbit with $a = 0.9M$, $p = 12$, $e = 0.2$, $I = 30°$.

m	l	n	k	$\mathrm{Re}\{C^+_{S,lmnk}\}$	$\mathrm{Im}\{C^+_{S,lmnk}\}$	$\mathrm{Re}\{C^-_{S,lmnk}\}$	$\mathrm{Im}\{C^-_{S,lmnk}\}$
1	2	0	1	4.8962×10^{-6}	-1.6020×10^{-6}	-5.2716×10^{-6}	-2.7823×10^{-7}
1	2	1	1	9.9514×10^{-6}	-2.7846×10^{-6}	3.8592×10^{-6}	8.7391×10^{-7}
1	2	2	1	7.3027×10^{-6}	-2.1468×10^{-6}	3.7407×10^{-6}	7.8065×10^{-7}
1	2	3	1	3.6008×10^{-6}	-1.1232×10^{-6}	1.7742×10^{-6}	3.8842×10^{-7}
1	3	0	2	-9.4587×10^{-8}	1.3025×10^{-7}	-5.8770×10^{-7}	-4.1971×10^{-7}
1	3	1	2	-8.8801×10^{-7}	-1.7932×10^{-6}	-3.2098×10^{-7}	-2.1754×10^{-7}
1	3	2	2	-9.8569×10^{-7}	-1.9468×10^{-6}	-1.1060×10^{-7}	-6.4897×10^{-8}
1	3	3	2	-6.6574×10^{-7}	-1.2388×10^{-6}	-3.7354×10^{-8}	-1.4854×10^{-8}
2	2	0	0	-1.9890×10^{-5}	5.8986×10^{-6}	-7.5636×10^{-6}	-3.6977×10^{-6}
2	2	1	0	-3.6535×10^{-5}	1.0473×10^{-5}	-2.8727×10^{-5}	-9.5114×10^{-6}
2	2	2	0	-2.8239×10^{-5}	8.6430×10^{-6}	-2.1354×10^{-5}	-7.5839×10^{-6}
2	2	3	0	-1.5302×10^{-5}	4.9730×10^{-6}	-1.0601×10^{-5}	-4.1408×10^{-6}
2	3	0	1	8.2420×10^{-7}	9.2288×10^{-7}	6.8449×10^{-7}	1.3381×10^{-6}
2	3	1	1	3.8727×10^{-6}	7.7467×10^{-6}	-1.2893×10^{-7}	-2.4943×10^{-7}
2	3	2	1	4.3094×10^{-6}	8.2104×10^{-6}	-4.2520×10^{-7}	-8.2810×10^{-7}
2	3	3	1	3.0636×10^{-6}	5.4471×10^{-6}	-3.3219×10^{-7}	-6.4545×10^{-7}
3	3	0	0	-2.2312×10^{-6}	-3.3582×10^{-6}	-3.0967×10^{-7}	-1.2954×10^{-6}
3	3	1	0	-8.9746×10^{-6}	-1.7781×10^{-5}	5.0351×10^{-7}	3.8648×10^{-6}
3	3	2	0	-1.0099×10^{-5}	-1.8845×10^{-5}	6.2534×10^{-7}	4.8041×10^{-6}
3	3	3	0	-7.3942×10^{-6}	-1.2830×10^{-5}	4.0686×10^{-7}	3.3295×10^{-6}
3	4	0	1	1.1671×10^{-6}	-4.1185×10^{-7}	1.9807×10^{-7}	-2.0808×10^{-7}
3	4	1	1	-3.6720×10^{-6}	2.6844×10^{-6}	4.2934×10^{-8}	-4.2764×10^{-8}
3	4	2	1	-5.6428×10^{-6}	4.2331×10^{-6}	-8.4756×10^{-8}	9.4155×10^{-8}
3	4	3	1	-4.6912×10^{-6}	3.7655×10^{-6}	-1.0502×10^{-7}	1.1655×10^{-7}

[1] P. Amaro-Seoane, H. Audley, S. Babak, J. Baker, E. Barausse, P. Bender, E. Berti, P. Binetruy, M. Born, D. Bortoluzzi, J. Camp, C. Caprini *et al.*, Laser interferometer space antenna, arXiv:1702.00786.

[2] J. Luo, L.-S. Chen, H.-Z. Duan, Y.-G. Gong, S. Hu, J. Ji, Q. Liu, J. Mei, V. Milyukov, M. Sazhin, C.-G. Shao, V. T. Toth, H.-B. Tu, Y. Wang, Y. Wang, H.-C. Yeh, M.-S. Zhan, Y. Zhang, V. Zharov, and Z.-B. Zhou, TianQin: A space-borne gravitational wave detector, Classical Quantum Gravity **33,** 035010 (2016).

[3] W.-H. Ruan, Z.-K. Guo, R.-G. Cai, and Y.-Z. Zhang, Taiji program: Gravitational-wave sources, Int. J. Mod. Phys. A **35,** 2050075 (2020).

[4] S. Babak, J. Gair, A. Sesana, E. Barausse, C. F. Sopuerta, C. P. L. Berry, E. Berti, P. Amaro-Seoane, A. Petiteau, and A. Klein, Science with the space-based interferometer LISA. V. Extreme mass-ratio inspirals, Phys. Rev. D **95,** 103012 (2017).

[5] E. Poisson, A. Pound, and I. Vega, The motion of point particles in curved spacetime, Living Rev. Relativity **14,** 7 (2011).

[6] A. Pound and B. Wardell, Black hole perturbation theory and gravitational self-force, in *Handbook of Gravitational Wave Astronomy*, edited by C. Bambi, S. Katsanevas, and K. D. Kokkotas (Springer Singapore, Singapore, 2020), pp. 1–119.

[7] L. Barack and A. Pound, Self-force and radiation reaction in general relativity, Rep. Prog. Phys. **82,** 016904 (2019).

[8] T. Hinderer and É. É. Flanagan, Two-timescale analysis of extreme mass ratio inspirals in Kerr spacetime: Orbital motion, Phys. Rev. D **78,** 064028 (2008).

[9] J. Miller and A. Pound, Two-timescale evolution of extreme-mass-ratio inspirals: Waveform generation scheme for quasicircular orbits in Schwarzschild spacetime, Phys. Rev. D **103,** 064048 (2021).

[10] R. Fujita and M. Shibata, Extreme mass ratio inspirals on the equatorial plane in the adiabatic order, Phys. Rev. D **102,** 064005 (2020).

[11] S. A. Hughes, N. Warburton, G. Khanna, A. J. K. Chua, and M. L. Katz, Adiabatic waveforms for extreme mass-ratio inspirals via multivoice decomposition in time and frequency, Phys. Rev. D **103,** 104014 (2021).

[12] V. Skoupý and G. Lukes-Gerakopoulos, Adiabatic equatorial inspirals of a spinning body into a Kerr black hole, Phys. Rev. D **105,** 084033 (2022).

[13] S. Isoyama, R. Fujita, A. J. K. Chua, H. Nakano, A. Pound, and N. Sago, Adiabatic Waveforms from Extreme-Mass-Ratio Inspirals: An Analytical Approach, Phys. Rev. Lett. **128,** 231101 (2022).

[14] M. D. Hartl, Dynamics of spinning test particles in Kerr spacetime, Phys. Rev. D **67,** 024005 (2003).

[15] N. Sago, T. Tanaka, W. Hikida, K. Ganz, and H. Nakano, Adiabatic evolution of orbital parameters in Kerr spacetime, Prog. Theor. Phys. **115,** 873 (2006).

[16] S. Akcay, S. R. Dolan, C. Kavanagh, J. Moxon, N. Warburton, and B. Wardell, Dissipation in extreme mass-ratio binaries with a spinning secondary, Phys. Rev. D **102,** 064013 (2020).

[17] J. Mathews, A. Pound, and B. Wardell, Self-force calculations with a spinning secondary, Phys. Rev. D **105,** 084031 (2022).

[18] V. Witzany, J. Steinhoff, and G. Lukes-Gerakopoulos, Hamiltonians and canonical coordinates for spinning particles in curved space-time, Classical Quantum Gravity **36,** 075003 (2019).

[19] R. Rüdiger, Conserved quantities of spinning test particles in general relativity. I, Proc. R. Soc. A **375,** 185 (1981).

[20] R. Rüdiger, Conserved quantities of spinning test particles in general relativity. II, Proc. R. Soc. A **385,** 229 (1981).

[21] V. Witzany, Hamilton-Jacobi equation for spinning particles near black holes, Phys. Rev. D **100,** 104030 (2019).

[22] B. Carter, Global structure of the Kerr family of gravitational fields, Phys. Rev. **174,** 1559 (1968).

[23] C. Cutler, D. Kennefick, and E. Poisson, Gravitational radiation reaction for bound motion around a Schwarzschild black hole, Phys. Rev. D **50,** 3816 (1994).

[24] L. S. Finn and K. S. Thorne, Gravitational waves from a compact star in a circular, inspiral orbit, in the equatorial plane of a massive, spinning black hole, as observed by lisa, Phys. Rev. D **62,** 124021 (2000).

[25] K. Glampedakis and D. Kennefick, Zoom and whirl: Eccentric equatorial orbits around spinning black holes and their evolution under gravitational radiation reaction, Phys. Rev. D **66,** 044002 (2002).

[26] M. Shibata, Gravitational waves by compact star orbiting around rotating supermassive black holes, Phys. Rev. D **50,** 6297 (1994).

[27] S. Drasco and S. A. Hughes, Gravitational wave snapshots of generic extreme mass ratio inspirals, Phys. Rev. D **73,** 024027 (2006).

[28] W.-B. Han, Gravitational radiation from a spinning compact object around a supermassive Kerr black hole in circular orbit, Phys. Rev. D **82,** 084013 (2010).

[29] E. Harms, G. Lukes-Gerakopoulos, S. Bernuzzi, and A. Nagar, Asymptotic gravitational wave fluxes from a spinning particle in circular equatorial orbits around a rotating black hole, Phys. Rev. D **93,** 044015 (2016).

[30] E. Harms, G. Lukes-Gerakopoulos, S. Bernuzzi, and A. Nagar, Spinning test body orbiting around a Schwarzschild black hole: Circular dynamics and gravitational-wave fluxes, Phys. Rev. D **94,** 104010 (2016).

[31] G. Lukes-Gerakopoulos, E. Harms, S. Bernuzzi, and A. Nagar, Spinning test body orbiting around a Kerr black hole: Circular dynamics and gravitational-wave fluxes, Phys. Rev. D **96,** 064051 (2017).

[32] G. A. Piovano, A. Maselli, and P. Pani, Extreme mass ratio inspirals with spinning secondary: A detailed study of equatorial circular motion, Phys. Rev. D **102,** 024041 (2020).

[33] G. A. Piovano, R. Brito, A. Maselli, and P. Pani, Assessing the detectability of the secondary spin in extreme mass-ratio inspirals with fully relativistic numerical waveforms, Phys. Rev. D **104,** 124019 (2021).

[34] V. Skoupý and G. Lukes-Gerakopoulos, Gravitational wave templates from extreme mass ratio inspirals, arXiv:2101.04533.

[35] M. Rahman and A. Bhattacharyya, Prospects for determining the nature of the secondaries of extreme mass-ratio inspirals using the spin-induced quadrupole deformation, Phys. Rev. D **107,** 024006 (2023).

[36] V. Skoupý and G. Lukes-Gerakopoulos, Spinning test body orbiting around a Kerr black hole: Eccentric equatorial orbits and their asymptotic gravitational-wave fluxes, Phys. Rev. D **103,** 104045 (2021).

[37] L. V. Drummond and S. A. Hughes, Precisely computing bound orbits of spinning bodies around black holes. I. General framework and results for nearly equatorial orbits, Phys. Rev. D **105,** 124040 (2022).

[38] L. V. Drummond and S. A. Hughes, Precisely computing bound orbits of spinning bodies around black holes. II. Generic orbits, Phys. Rev. D **105,** 124041 (2022).

[39] M. Mathisson, Neue mechanik materieller systemes, Acta Phys. Pol. **6,** 163 (1937).

[40] M. Mathisson, Republication of: New mechanics of material systems, Gen. Relativ. Gravit. **42,** 1011 (2010).

[41] W. Dixon, Isolated gravitating systems in general relativity, *Proceedings of the International School of Physics "Enrico Fermi," Course LXVII*, edited by J. Ehlers (North Holland, Amsterdam (1979), 156.

[42] A. Papapetrou, Spinning test particles in general relativity. 1., Proc. R. Soc. A **209,** 248 (1951).

[43] W. Dixon, Dynamics of extended bodies in general relativity. I. Momentum and angular momentum, Proc. R. Soc. A **314,** 499 (1970).

[44] W. Tulczyjew, Motion of multipole particles in general relativity theory, Acta Phys. Pol. **18,** 393 (1959).

[45] J. Ehlers and E. Rudolph, Dynamics of extended bodies in general relativity center-of-mass description and quasirigidity, Gen. Relativ. Gravit. **8,** 197 (1977).

[46] S. Suzuki and K.-I. Maeda, Chaos in Schwarzschild spacetime: The motion of a spinning particle, Phys. Rev. D **55,** 4848 (1997).

[47] M. Visser, The Kerr spacetime: A brief introduction, arXiv:0706.0622.

[48] O. Zelenka, G. Lukes-Gerakopoulos, V. Witzany, and O. Kopáček, Growth of resonances and chaos for a spinning test particle in the Schwarzschild background, Phys. Rev. D **101,** 024037 (2020).

[49] J.-A. Marck, Solution to the equations of parallel transport in Kerr geometry; tidal tensor, Proc. R. Soc. A **385,** 431 (1983).

[50] M. van de Meent, Analytic solutions for parallel transport along generic bound geodesics in Kerr spacetime, Classical Quantum Gravity **37**, 145007 (2020).

[51] R. Fujita and W. Hikida, Analytical solutions of bound timelike geodesic orbits in Kerr spacetime, Classical Quantum Gravity **26**, 135002 (2009).

[52] S. A. Teukolsky, Perturbations of a rotating black hole. 1. Fundamental equations for gravitational electromagnetic and neutrino field perturbations, Astrophys. J. **185**, 635 (1973).

[53] T. Tanaka, Y. Mino, M. Sasaki, and M. Shibata, Gravitational waves from a spinning particle in circular orbits around a rotating black hole, Phys. Rev. D **54**, 3762 (1996).

[54] Black Hole Perturbation Toolkit, http://bhptoolkit.org/, 2023.

[55] S. Hopper, E. Forseth, T. Osburn, and C. R. Evans, Fast spectral source integration in black hole perturbation calculations, Phys. Rev. D **92**, 044048 (2015).

[56] R. P. Macedo, B. Leather, N. Warburton, B. Wardell, and A. Zenginoğlu, Hyperboloidal method for frequency-domain self-force calculations, Phys. Rev. D **105**, 104033 (2022).

[57] S. Mano, H. Suzuki, and E. Takasugi, Analytic solutions of the Teukolsky equation and their low frequency expansions, Prog. Theor. Phys. **95**, 1079 (1996).

[58] E. W. Leaver, An analytic representation for the quasi-normal modes of Kerr black holes, Proc. R. Soc. A **402**, 285 (1985).

[59] M. Kerachian, L. Polcar, V. Skoupý, C. Efthymiopoulos, and G. Lukes-Gerakopoulos, Action-angle formalism for extreme mass ratio inspirals in Kerr spacetime, arXiv:2301.08150.

[60] N. Sago and R. Fujita, Calculation of radiation reaction effect on orbital parameters in Kerr spacetime, Prog. Theor. Exp. Phys. **2015**, 073E03 (2015).

[61] E. Harms, S. Bernuzzi, A. Nagar, and A. Zenginoglu, A new gravitational wave generation algorithm for particle perturbations of the Kerr spacetime, Classical Quantum Gravity **31**, 245004 (2014).

[62] M. van de Meent, Gravitational self-force on generic bound geodesics in Kerr spacetime, Phys. Rev. D **97**, 104033 (2018).

[63] B. Wardell, A. Pound, N. Warburton, J. Miller, L. Durkan, and A. Le Tiec, Gravitational Waveforms for Compact Binaries from Second-Order Self-Force Theory, Phys. Rev. Lett. **130**, 241402 (2023).

[64] P. Lynch, M. van de Meent, and N. Warburton, Eccentric self-forced inspirals into a rotating black hole, Classical Quantum Gravity **39**, 145004 (2022).

[65] G. Lukes-Gerakopoulos, J. Seyrich, and D. Kunst, Investigating spinning test particles: Spin supplementary conditions and the Hamiltonian formalism, Phys. Rev. D **90**, 104019 (2014).